# Thermochronology, geochronology, and upper crustal structure of the Cordillera Real: Implications for Cenozoic exhumation of the central Andean plateau

Robert J. Gillis,[1,2] Brian K. Horton,[1,3] and Marty Grove[1]

[1] Structural mapping, $^{40}Ar/^{39}Ar$ and fission track thermochronology, U-Pb geochronology, and basin analysis reveal rapid cooling during middle Eocene–late Oligocene and late Miocene–Pliocene exhumation in the central Andean plateau of Bolivia. In the 4–6 km high Cordillera Real, numerous granites and SW directed fold-thrust structures define the central Andean backthrust belt along the Altiplano–Eastern Cordillera boundary. U-Pb zircon analyses indicate Permo-Triassic granitic magmatism, with less extensive magmatism of late Oligocene age. Mapping reveals low magnitudes of slip (<2–5 km) for most faults on the basis of unit thicknesses, stratigraphic separation, and cutoff relationships. These results suggest that a deeper structure was probably involved in exhumation of rocks from >5 km depth. The ~26 Ma Quimsa Cruz granite postdated most thrust structures, suggesting that upper crustal shortening in the Cordillera Real had largely ceased by late Oligocene time. Results of $^{40}Ar/^{39}Ar$ and fission track modeling help constrain the moderate to low-temperature (<350°C) cooling history, revealing two phases of rapid cooling from 45–40 Ma to 26 Ma and from ~11 Ma onward. Initial cooling coincided with middle Eocene–late Oligocene deformation in the backthrust belt and associated deposition of coarse clastic sediments in the Altiplano basin. Eocene-Oligocene exhumation of ~7.5 km of upper crust is estimated on the basis of thermochronologic data. Rapid late Miocene and younger cooling involved an estimated ~3.5 km of exhumation and occurred in the apparent absence of upper crustal shortening. These findings suggest that crustal shortening and resultant exhumation of middle Eocene–late Oligocene age played a major role in construction of the central Andes. However, for late Miocene exhumation, the importance of alternative, nonshortening mechanisms is difficult to ascertain due to a poor understanding of subsurface structures. We speculate that greater precipitation on the eastern edge of the central Andean plateau north of ~17.5°S was a key factor in driving rapid, youthful exhumation of the Cordillera Real. **Citation:** Gillis, R. J., B. K. Horton, and M. Grove (2006), Thermochronology, geochronology, and upper crustal structure of the Cordillera Real: Implications for Cenozoic exhumation of the central Andean plateau, *Tectonics*, *25*, TC6007, doi:10.1029/2005TC001887.

## 1. Introduction

[2] The Cordillera Real forms high topography in one of the most intensely shortened and thickened region of the Andes [*Dorbath et al.*, 1993; *Baby et al.*, 1997; *Beck and Zandt*, 2002]. At 4–6.4 km altitude, the range marks both the eastern topographic margin of the central Andean plateau, defined as the low-relief, generally internally drained region above 3 km [*Isacks*, 1988], and the structural boundary between the Altiplano and Eastern Cordillera provinces (Figure 1). As the principal divide separating the closed Altiplano basin and Amazon drainage system, the Cordillera Real has profoundly influenced orographic precipitation, regional climate, and geomorphic evolution of the central Andes [*Masek et al.*, 1994; *Horton*, 1999; *Montgomery et al.*, 2001]. The range also occupies the transition from hinterland- to foreland-directed thrust structures [*McQuarrie and DeCelles*, 2001; *McQuarrie*, 2002] and coincides with a lithospheric boundary possibly representing an ancient suture zone [*Dorbath et al.*, 1993]. Furthermore, uplift of the Cordillera Real presumably helped dictate the Cenozoic sedimentation history of the Altiplano [*Sempere et al.*, 1990; *Horton et al.*, 2001, 2002].

[3] Despite its fundamental role in construction of the central Andean plateau, the timing, magnitude, and style of deformation, and associated exhumation and basin development remain poorly understood. Multiple granitic bodies compose the Cordillera Real, but disagreement persists over emplacement ages and subsequent cooling histories [e.g., *McBride et al.*, 1983; *Miller*, 1988; *Miller and Harris*, 1989; *Lamb and Hoke*, 1997]. Previous thermochronologic results, notably the fission track data of *Benjamin et al.* [1987], have been variably interpreted to suggest an Eocene

[1]Department of Earth and Space Sciences, University of California, Los Angeles, California, USA.
[2]Now at the Alaska Division of Geological and Geophysical Surveys, Fairbanks, Alaska, USA.
[3]Now at the Department of Geological Sciences and Institute for Geophysics, Jackson School of Geosciences, University of Texas at Austin, Austin, Texas, USA.
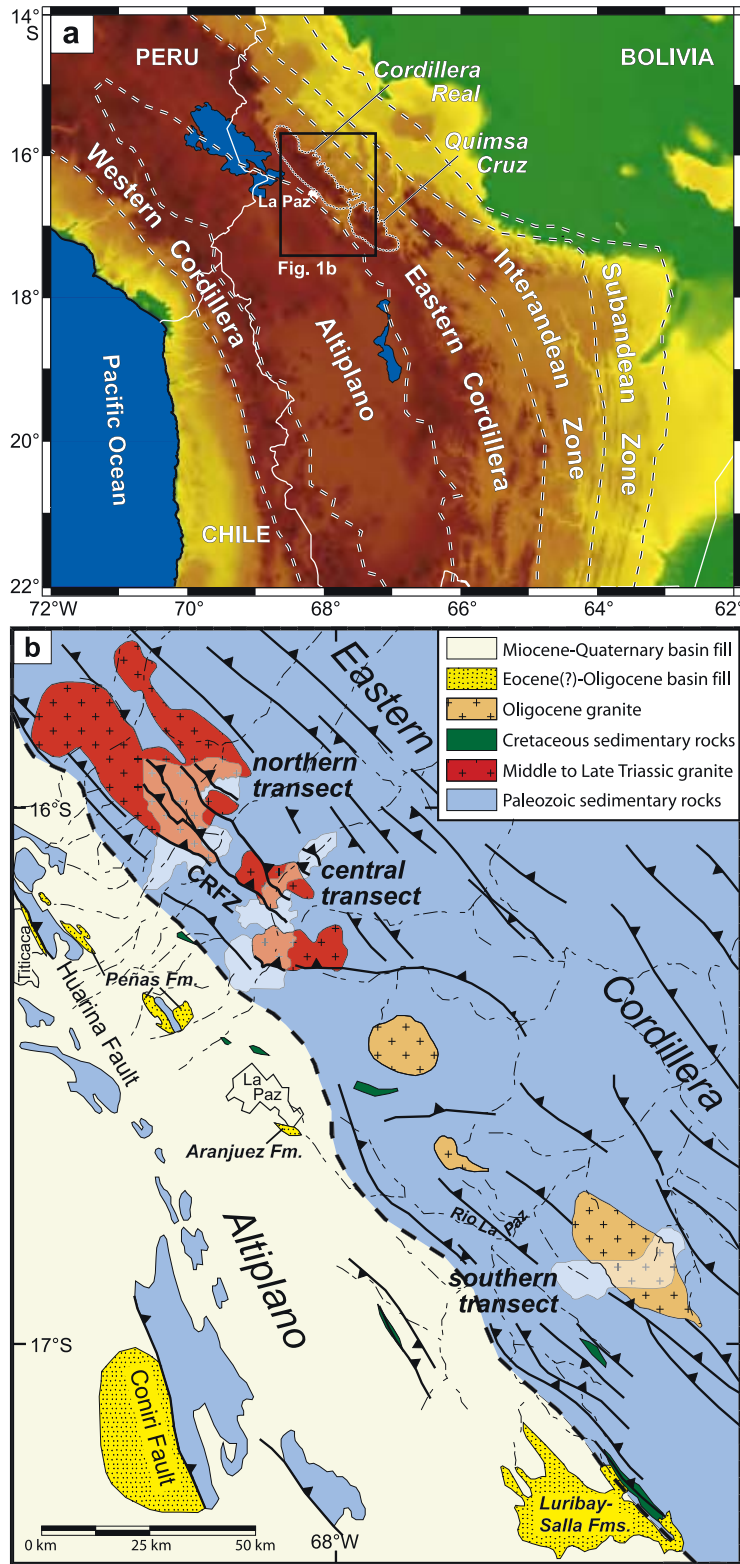
**Figure 1**

pulse of heating, Eocene pulse of cooling, uniform Eocene to modern cooling, Miocene linear or stepwise increase in cooling, and late Miocene exponential increase in cooling [*Benjamin*, 1986; *Benjamin et al.*, 1987; *Masek et al.*, 1994; *Lamb and Hoke*, 1997; *Safran*, 1998; *Moore and England*, 2001; *Anders et al.*, 2002]. These conflicting interpretations demonstrate the large uncertainties in the exhumation history of the Cordillera Real. An accurate record is essential for understanding mountain building and plateau evolution in the central Andes, and the interactions among tectonics, erosion, and climate.

[4] The purpose of this paper is to evaluate the exhumation record of the Cordillera Real along three mapping traverses at 16–17°S. Widespread granite exposures afford opportunities to assess the range's cooling history and crosscutting relationships with newly identified structures. U-Pb zircon analyses constrain Permo-Triassic and late Oligocene granite emplacement ages, and $^{40}Ar/^{39}Ar$, apatite fission track, and applicable modeling results provide a record of exhumation-induced cooling. These results indicate rapid cooling during middle Eocene to early Miocene time, considerably earlier than generally assumed. Exhumation of this age is consistent with sediment provenance data for clastic fill in the northern Altiplano basin dated between 34 and 24 Ma by new $^{40}Ar/^{39}Ar$ results for interbedded tuffs. Collectively, these findings require revision of previous estimates for the timing of initial topographic expression and tempo of exhumation along the eastern margin of the central Andean plateau.

## 2. Geologic Setting

[5] The Cordillera Real is a $30 \times 250$ km range along the eastern flank of the central Andean plateau (Figure 1). This rugged, glaciated range represents the highest nonvolcanic topography in Bolivia, with average elevations of ~5 km and major peak elevations of 6.1–6.4 km. Although it forms the NW trending divide between the Amazon drainage and internally drained Altiplano, the range has been breached locally by headward erosion of the Rio La Paz, a tributary of the Amazon. The entire range is recognized as the Cordillera Real, but high topography southeast of the Rio La Paz is commonly identified separately as the Quimsa Cruz (Figure 1a).

[6] The Cordillera Real lies within the Huarina fold-thrust belt (HFTB) of the westernmost Eastern Cordillera (Figure 1). The HFTB represents part of the W to SW directed central Andean backthrust belt that extends from 15 to 22°S in the hinterland of the central Andes [*Newell*, 1949; *Pareja et al.*, 1978; *Martinez*, 1980; *Roeder*, 1988; *Sempere et al.*, 1990; *McQuarrie and DeCelles*, 2001]. Ordovician strata are the structurally lowest rocks exposed and define an axis between a NE directed thrust system and the SW directed backthrust belt. Younger rocks in the HFTB include

Upper Devonian with limited Carboniferous and Cretaceous rocks. Frontal thrusts of the HFTB, including the SW directed Huarina and Coniri faults (Figure 1b), place Paleozoic rocks on mainly mid-Cenozoic strata, but are commonly covered by younger Altiplano fill [*Sempere et al.*, 1990; *Marsh et al.*, 1992].

[7] In this study, three NE-SW transects were mapped at 1:50,000 scale to provide shortening estimates and a structural framework for interpreting thermochronologic results. The 20–40 km long transects are orthogonal to structural trends and continue northeastward from the Altiplano margin. The northern (Amaguaya), central (Rio Zongo), and southern (Quimsa Cruz) traverses contain similar structures and extensive granites that intrude mainly Ordovician-Silurian rocks (Figures 2 and 3). Low-grade metamorphic conditions affected Paleozoic strata, producing slate, phyllite, and minor quartzite [*Martinez*, 1980]. The main stratigraphic units include: Upper Ordovician Coroico (~2300 m) and Amutara (~800–3300 m) formations; Silurian Cancañiri (~100–335 m), Uncia (~900–1300 m), and Catavi (480–600 m) formations; Devonian Vila Vila Formation (~700–850 m); and local occurrences of Carboniferous, Permian, and Cretaceous units [*Servicio Geológico de Bolivia (Geobol)*, 1993, 1995, 1997; *McQuarrie and DeCelles*, 2001]. Major décollement horizons are in the Coroico, Uncia, and Cancañiri formations.

[8] Granites in the Cordillera Real are of Permo-Triassic and mid-Cenozoic age. In the north, four Permo-Triassic intrusions occupy the highest parts of the range: the Illampu and Yani plutons in the northern transect and the Huayna Potosí and Zongo plutons in the central transect (Figure 2). Although not continuously exposed, these mineralogically similar two-mica granites may be genetically related [*McBride et al.*, 1983]. Whereas the Illampu and Huayna Potosí granites are generally nonfoliated and medium-grained, the Zongo granite is much coarser with a pervasive NE dipping foliation; foliation in the medium-grained Yani granite only occurs locally along its NE margin. In the south, the Quimsa Cruz pluton cuts Paleozoic rocks (Figure 3) and is composed of a nonfoliated granodiorite and a porphyritic monzogranite.

## 3. Structural Geology

[9] Three mapping transects (Figures 1–3) were selected to maximize exposure, relief, and accessibility. Most structures fall into three categories: (1) NE dipping faults cutting Paleozoic strata with hanging wall on footwall thrust cutoff geometries ranging from ramp on ramp to flat on flat; (2) steeply NE dipping faults cutting granites with possible hanging wall ramp on footwall ramp thrust relationships; and (3) fault-bend, fault propagation, and buckle folds in Paleozoic strata. Tentative fault slip estimates are made on

**Figure 1.** (a) Regional topography of the central Andes showing boundaries (dashed lines) between major tectonomorphic zones [after *McQuarrie et al.*, 2005a]. Darker colors define high topography (>4.5 km) of Cordillera Real. (b) Regional geologic map of the Cordillera Real and surrounding regions of the central Andean backthrust belt along the Eastern Cordillera–Altiplano boundary. Areas of white shading show extent of three mapping transects. CRFZ, Cordillera Real fault zone.
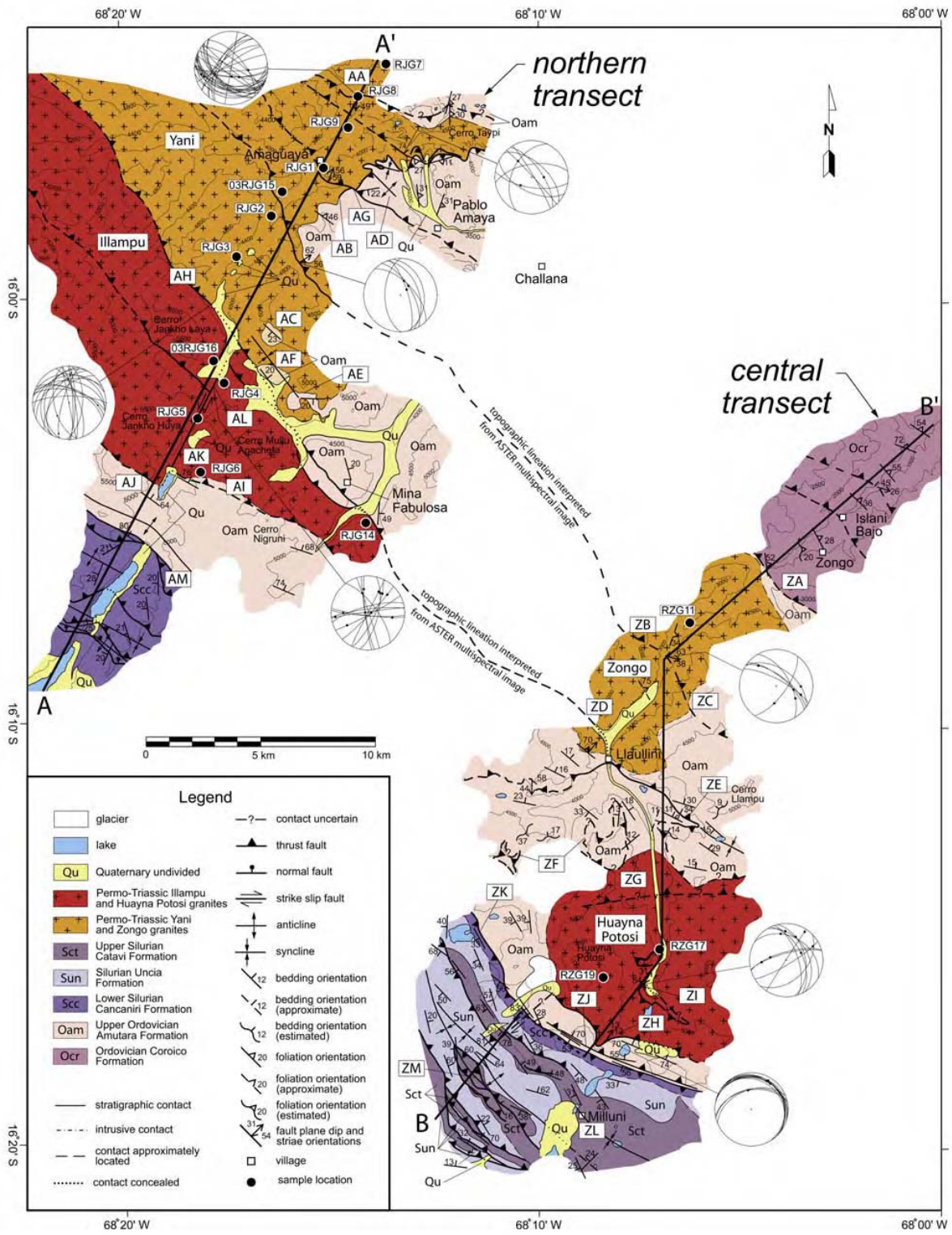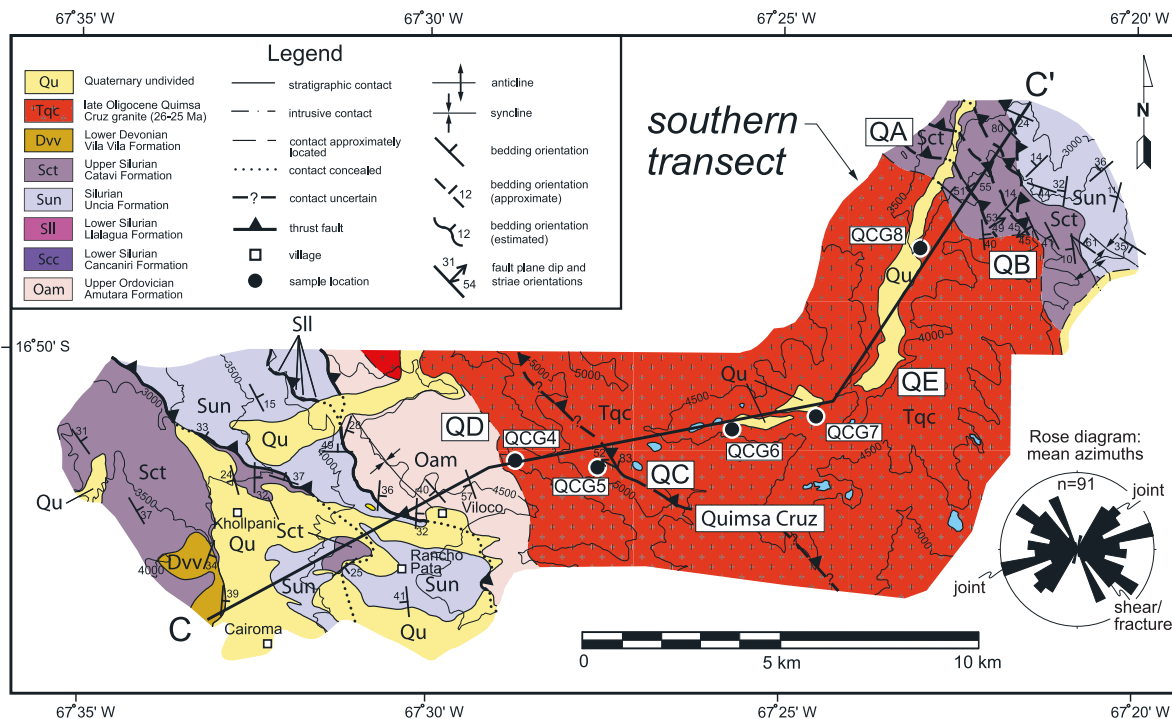
**Figure 2**

**Figure 3.** Geologic map of southern (Quimsa Cruz) transect. Location is shown in Figure 1b. Black circles identify granite samples for thermochronologic studies. Lettered rectangles (QA–QE) identify locations discussed in text. Rose diagram represents joint and fracture orientations.

the basis of stratigraphic separation, unit thicknesses, fault cutoff relationships, and inferred geometries at depth. Cross sections (Figure 4) are not balanced and are presented only as representations compatible with mapped surface structures; alternative interpretations are permissible.

### 3.1. Northern Transect: Amaguaya Region

[10] Permo-Triassic granites intrude the Ordovician Amutara Formation (Oam) and are cut by steeply NE dipping thrusts along the northern transect. The moderately SW dipping Amaguaya thrust marks the northern edge of the transect (Figures 2 and 4a). A prominent fault in the middle of the transect places the Yani pluton over the Illampu pluton; regionally, this fault separates gently dipping Oam strata and low-amplitude fold trains in the NE from steeply NE dipping Oam strata in the SW (Figure 2). The southern edge of the transect consists of folded and thrusted slates of the Silurian Cancañiri Formation (Scc) along the eastern margin of the Altiplano. The lack of cutoffs within granites and stratigraphic uncertainties preclude shortening estimates for this transect.

#### 3.1.1. NE Part: Amaguaya Thrust

[11] The principal NE directed thrust in the region cuts the NE margin of the Yani pluton (AA, Figure 2). This fault,

here named the Amaguaya thrust, is defined by a SW dipping (49–54°) ~10–20 cm wide ductile shear zone enveloped within an ~200 m wide brittle shear zone. In both hanging wall and footwall, pervasive fractures and a well-developed foliation in the Yani granite dip 20–70°SW. Shear sense indicators and slickenlines (stereonets, Figure 2) indicate top-to-NE transport. In map view, the fault trace projects to the ESE into shallowly dipping Ordovician Amutara (Oam) strata that occur in both hanging wall and footwall, suggesting limited stratigraphic separation. A lack of Oam marker horizons precludes slip estimates.

#### 3.1.2. ENE Part: Ordovician Rocks

[12] The ENE part of the transect is dominated by shallowly dipping Oam strata. Oam is in intrusive contact with the Yani granite (AB, Figure 2) except near the NE edge of the transect where it is in fault contact along a SW dipping thrust fault. The intrusive Oam-Yani contact parallels bedding and dips ~4°NE over a ~10 km distance (AB and AC). Low-amplitude NW trending folds are common in Oam strata to the NE (AD). In the SSE, the Yani granite intruded gently folded Oam strata (AC and AE) considered to be the roof of the Yani pluton (AF). A potential Yani roof contact (AB) is truncated by a NE dipping fault (AG) with only ~60 m of throw.

**Figure 2.** Geologic maps of northern (Amaguaya) and central (Rio Zongo) transects. Location is shown in Figure 1b. Black circles identify granite samples for thermochronologic studies. Lettered rectangles (AA–AM; ZA–ZM) identify locations discussed in text. Stereonets represent fault orientation and slickenline data.
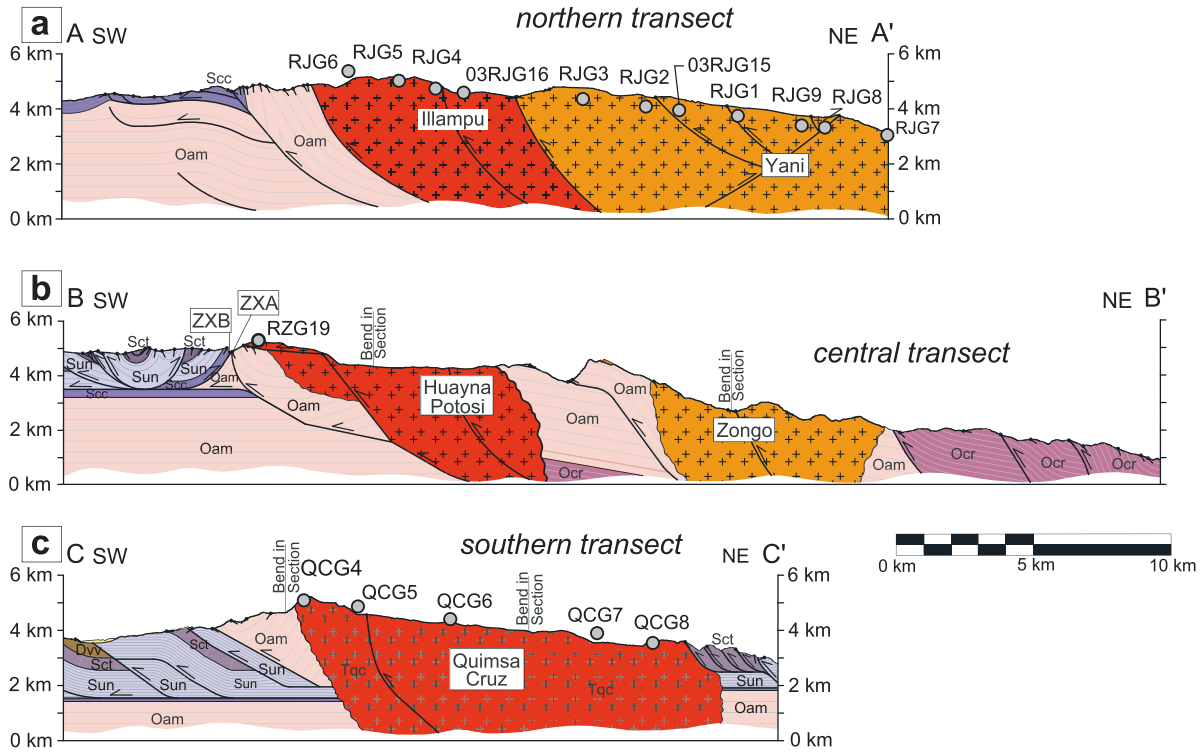
**Figure 4.** Schematic cross sections of mapped transects (locations shown in Figures 2 and 3). (a) Northern (Amaguaya) transect. (b) Central (Rio Zongo) transect. (c) Southern (Quimsa Cruz) transect.

### 3.1.3. Middle Part: Yani-Illampu Thrust

[13] A major NE dipping (∼63°) fault juxtaposes the Yani and Illampu plutons (AH, Figure 2). This structure, the Yani-Illampu thrust, continues >170 km to the NW and places Ordovician over Devonian rocks [*Servicio Nacional de Geología y Técnico de Minas and Yacimientos Petrolíferos Fiscales Bolivianos*, 2003], a minimum stratigraphic separation of ∼5 km. Displacement decreases to the SE, with the Zongo granite and Oam strata thrust onto Oam rocks in a hanging wall flat on footwall ramp cutoff relationship in the central transect (ZD, Figure 2).

### 3.1.4. SW Margin of Illampu Granite

[14] The SW margin of the Illampu pluton is generally in fault contact with steeply NE dipping Oam strata. A NE dipping (∼75°) strand of this fault (AI, Figure 2) is defined by fracture and gouge zones exhibiting slickensides of variable orientation. To the NW, the fault has been displaced ∼1 km by a NE striking left-lateral fault (AJ), consistent with centimeter-scale left-lateral shear indicators (AK) and NE striking subvertical fractures with gently NE plunging lineations (AL).

### 3.1.5. SW Part: Paleozoic Rocks

[15] Steeply NE dipping strata in the SW are potentially overturned near the Ordovician-Silurian contact (AM, Figure 2), although mud-draped ripple marks in the Silurian Cancañiri Formation (Scc) show upright orientations locally. A proposed fault placing overturned, steeply NE dipping

Scc hanging wall rocks over relatively flat-lying Scc strata accommodated an unknown amount of slip.

### 3.2. Central Transect: Rio Zongo Region

[16] Mapping of a series of NE dipping thrusts and the Permo-Triassic Zongo and Huayna Potosí granites along the central transect helps place thermochronologic data [e.g., *McBride et al.*, 1983, 1987; *Benjamin et al.*, 1987] into a structural context (Figure 2 and 4b). Ordovician-Silurian strata and the two plutons are well exposed at high elevation, but mapping in more vegetated areas below ∼3.5 km was performed primarily by roadcut inspection along the Zongo valley. Here, faults were identified locally and tentatively projected along strike using measured orientations, topographic features, and satellite imagery.

### 3.2.1. NE Part: Zongo Granite

[17] In the NE, the Zongo pluton, Ordovician Coroico (Ocr), and Amutara (Oam) formations are deformed by SW directed thrusts. Displacement is difficult to constrain, but unit thicknesses indicate <2.5 km of stratigraphic separation for faults placing Ocr on footwall Ocr and Oam strata (ZA, Figure 2) [*Geobol*, 1995]. The Zongo granite intruded Oam rocks along its NE and SW margins [*Heinrich*, 1988] and is bisected by a NE dipping (63°) fault (ZB) that produced minimal offset of the SE pluton margin (ZC). Along its SW margin, the Zongo granite is cut by a NE dipping fault (ZD) that correlates with the Yani-Illampu thrust to the north (AH,

Figure 2). The SE continuation of this fault is unclear, but probably links with a fault in Oam strata (ZE).

### 3.2.2. Middle Part: Paleozoic Rocks

[18] South of the Zongo pluton, a SW directed thrust places an Oam hanging wall flat on an Oam footwall ramp (ZE, Figure 2). Hanging wall klippen are preserved ~3 km SSW of the main fault trace (ZF). Mapped traces of the klippen are estimated on the basis of bedding-parallel fractures and bedding discordances observed from neighboring ridges. Correlation of the main fault trace and klippen suggests a NE to SW change in the footwall from a 30°N dipping ramp to an 11°N dipping flat. These relationships reveal a minimum displacement of ~6.5 km, suggesting that this fault is one of the larger magnitude structures of the region.

### 3.2.3. NE Margin of Huayna Potosí Granite

[19] The trace of the northern contact of the Huayna Potosí pluton across the Zongo valley and flanking ridges (ZG, Figure 2) is consistent with a N dipping contact. However, a localized <10 m wide fracture between granite and Oam strata dips ~65°SE with E trending striae, inconsistent with the mapped geometry. Additionally, both the granite and Oam rocks occur locally on both sides of the fracture. Therefore the N margin of the Huayna Potosí granite is not considered a major structure and is tentatively interpreted to be a modified intrusive contact with limited thrust or strike-slip displacement.

### 3.2.4. SW Margin of Huayna Potosí Granite

[20] Along its SW edge, the Huayna Potosí granite sits in the hanging wall of a low-angle (13°), NE dipping fault that cuts NE dipping Oam strata (ZH, Figure 2). NE plunging fault striae indicate transport to the SW. The fault cuts downsection to the SW across steeply dipping footwall strata, suggesting out-of-sequence motion. In map view, the fault defines a small salient (ZH), requiring >1 km of heave. A structural window reveals the NE continuation of the thrust (ZI), exposing a transition to a NE dipping (54°) footwall ramp where the Huayna Potosí granite occurs in both hanging wall and footwall.

### 3.2.5. Ordovician-Silurian Contact

[21] Southwest of the Huayna Potosí granite, structures near the Ordovician-Silurian contact include a SW vergent, thrust-cored anticline with steeply NE dipping Oam strata on the NE limb. On the SW limb, Oam rocks are locally overturned (ZJ, Figure 2) with overlying, SW dipping Scc strata commonly exhibiting hematitic mineralization along the basal contact (ZK). The anticline dies out along strike to the NW (ZJ). Kinematic indicators below the mineralized contact include meter-scale, NE directed, ramp and flat fault geometries and top-to-NE folds (ZK). Mineralization and deformation may be related to bedding-parallel flexural slip associated with SW vergent folding or tectonic wedging of competent Oam quartzite beneath the Scc shale (ZXA, Figure 4b). The minimum shortening produced by the exposed fault propagation fold is 400 m, but wedge emplacement may have accommodated several additional kilometers.

### 3.2.6. SW Part: Paleozoic Rocks

[22] The dominant structures in the SW include two faulted synclines containing the Silurian Catavi Formation (Sct) in their cores (ZL and ZM, Figure 2). Because the

Silurian Uncia Formation (Sun) appears to be relatively thin (~870 m) in this area (ZXB, Figure 4b), the Uncia section must have been thickened in the southern syncline (ZM). Because Sun strata are tightly folded in this locality, the Sun was likely thickened by internal deformation. Net slip in the Silurian section is estimated at >5 km.

## 3.3. Southern Transect: Quimsa Cruz Region

[23] NW trending structures (Figures 3 and 4c) are concentrated in Paleozoic strata on the flanks of the mid-Cenozoic Quimsa Cruz pluton. Limited deformation affected the granite, which lacks foliation and truncates most NE dipping thrusts and associated folds.

### 3.3.1. NE Part: Paleozoic Rocks

[24] NE dipping panels of imbricated Silurian Uncia (Sun) and Catavi (Sct) strata are exposed near the NE margin of the Quimsa Cruz pluton (QA, Figure 3). Exposure is relatively poor, but a possible repetition of Sct rocks is interpreted on the basis of measured bedding orientations and an assumed 500 m original stratigraphic thickness. A prominent fault exposed near the NE margin of the granite dips NE (53°) with NE trending striae, but does not continue into the granite. A similar relationship is observed ~1 km to the east where the granite apparently cuts a NE dipping fault within the Sct section (QB).

### 3.3.2. Quimsa Cruz Granite

[25] Limited deformation of the Quimsa Cruz granite was recorded by rare, thin, discontinuous brittle shear zones that in some cases match linear topographic features, rare slickensides, or subvertical joints. One prominent topographic lineament tentatively interpreted as the trace of a steeply NE dipping fault parallels regional structures and extends across the pluton (QC, Figure 3), continuing into Paleozoic rocks to the SE. Brittle shear indicators in the pluton exhibit steep ~45–80° NW dips with N trending striae. Reconnaissance mapping of the SE segment of the lineament near the SE pluton margin (near Mina Caracoles) suggests abundant slickensides but little apparent offset of the intrusive contact.

[26] Although there is a continuum of steeply NW to NE dipping fractures in the pluton (rose diagram, Figure 3), many fractures strike ~125°, similar to regional structural trends. Possible joint faces striking ~045° and ~075° are expressed by uniform surfaces that form high cliffs and are better developed along the NE pluton margin and surrounding Paleozoic wall rocks.

### 3.3.3. SW Part: Paleozoic Rocks

[27] West of the Quimsa Cruz pluton, Ordovician–Devonian strata are deformed by SW directed thrusts that place older on successively younger rocks toward the SW. The granite cuts Ordovician Amutara (Oam) strata along the NE limb of a NW trending syncline (QD, Figure 3). The SW limb contains a thrust placing Oam on Sun strata in a hanging wall flat on footwall flat geometry, requiring ~3.4 km of minimum slip. Reported unit thicknesses [Geobol, 1997] suggest structural thickening of the Oam section, and Oam and Sun panels are in turn thrust over the Sct section in a flat on flat relationship that requires ~2 km of minimum slip. In the SW part of the transect, gently dipping Sun shales are
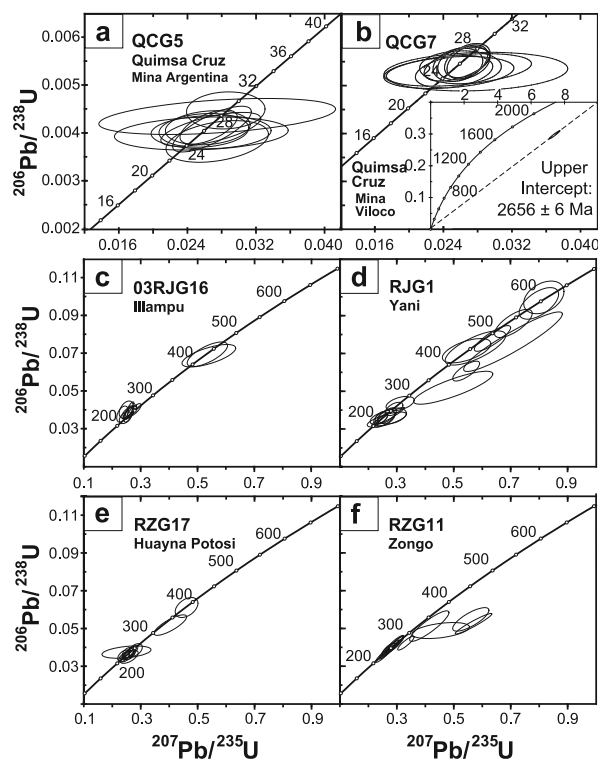
**Figure 5.** U-Pb concordia diagrams for analyzed zircon grains from Cordillera Real granites. Error ellipses are shown at $2\sigma$ level. (a) Quimsa Cruz (Mina Argentina) granodiorite. (b) Quimsa Cruz (Mina Viloco) porphyritic monzogranite. (c) Illampu granite. (d) Yani granite. (e) Huayna Potosí granite. (f) Zongo granite.

inferred to structurally overlie E dipping Sct and Devonian Vila Vila strata in an apparent hanging wall ramp on footwall flat relationship. The minimum estimated slip required to produce this geometry is ~2.7 km.

### 3.4. Summary

[28] Mapping and cross section construction reveal a complex array of Paleozoic strata and Mesozoic-Cenozoic granites involved in fold-thrust structures. Shear sense indicators and slickenline data indicate principally dip slip motion along NW striking, generally NE dipping faults (stereonets and rose diagram, Figures 2 and 3). Stratigraphic cutoff relationships are consistent with ramp and flat geometries. Therefore most faults are interpreted as thin-skinned, SW directed thrusts (Figure 4) developed during NE-SW shortening, consistent with previous studies of the central Andean backthrust belt [*Newell*, 1949; *Pareja et al.*, 1978; *Martinez*, 1980; *Roeder*, 1988; *Sempere et al.*, 1990; *Geobol*, 1993, 1995, 1997; *McQuarrie and DeCelles*, 2001].

[29] Structural relationships reveal low magnitudes of slip (<2–5 km) for most faults. Fault displacements are poorly constrained, particularly for granites, which lack cutoffs but were emplaced at 10–15 km depth (3–5 kbar) [*McBride et al.*, 1983; *Heinrich*, 1988]. Possible larger

magnitude structures potentially accommodated >5 km of reverse slip, including from NE to SW: (1) the NE directed Amaguaya thrust; (2) the SW directed Yani-Illampu thrust; (3) thrusts bounding the SW margins of the Illampu and Huayna Potosí granites; and (4) thrusts near the Ordovician-Silurian contact along the SW edges of the northern and central transects. Despite the uncertainties for individual structures, an estimation of total displacement suggests ~20 km of minimum cumulative slip, or ~35% NE-SW shortening. This minimum estimate of local strain is slightly lower than, but compatible with, the ~50% net strain suggested by recent estimates of regional shortening [*McQuarrie*, 2002; *Arriagada et al.*, 2005].

[30] Crosscutting relationships among thrusts and granites place timing constraints on deformation. The mid-Cenozoic Quimsa Cruz pluton truncates folds and thrusts along its margins (QB and QD, Figure 3) and is not cut by faults involving Permo-Triassic granites (Figure 2). The only postulated fault that cuts the Quimsa Cruz pluton continues into Paleozoic strata to the SE but produces limited offset of the intrusive contact [*Geobol*, 1997]. These observations indicate that most NE-SW shortening post-dated Permo-Triassic magmatism and predated mid-Cenozoic magmatism, supporting suggestions that the Quimsa Cruz granite was emplaced after the bulk of upper crustal shortening in the Eastern Cordillera [*Evernden et al.*, 1977; *Lamb and Hoke*, 1997].

## 4. U-Pb Geochronology

[31] New ion microprobe U-Pb analyses support previous K-Ar, $^{40}$Ar/$^{39}$Ar, and limited conventional U-Pb measurements indicating emplacement of most intrusions in the Cordillera Real during Permo-Triassic time [*Evernden et al.*, 1977; *McBride et al.*, 1983, 1987; *Farrar et al.*, 1988; *Heinrich*, 1988]. These include the Illampu (Sorata), Yani, Huayna Potosí (Chucara), Zongo, and Taquesa (Mururata) granites [*Evernden et al.*, 1977; *Martinez*, 1980; *McBride et al.*, 1983], which are partially synchronous with Permian granites along strike ~250 km to the NW in southern Peru [*Lancelot et al.*, 1978; *Carlier et al.*, 1982]. Our results also support Cenozoic emplacement ages for at least one granite in the region (Quimsa Cruz granite) [*Evernden et al.*, 1977; *McBride et al.*, 1983; *Miller*, 1988; *Miller and Harris*, 1989; *Kennan et al.*, 1995]. For this granite, previous K-Ar and $^{40}$Ar/$^{39}$Ar biotite ages of 34.2–22.8 Ma [*Evernden et al.*, 1977; *McBride et al.*, 1983; *Kennan et al.*, 1995] and an unpublished zircon fission track age of 38 Ma [*Lamb et al.*, 1997] were used to infer a crystallization age between middle Eocene and early Miocene time.

[32] Results of U-Pb ion microprobe analyses of 78 zircons from 7 granite samples (6–18 zircons per sample) are summarized in Figure 5 and Table 1. All uncertainties are reported as $1\sigma$ standard errors. Complete methods and tabulated data are presented in Table S1 (available as auxiliary material[1]). A general issue that impacts U-Pb analyses of the Permo-Triassic granitoids is that many

---

[1]Auxiliary material data sets are available at ftp://ftp.agu.org/apend/tc/ 2005tc001887. Other auxiliary material files are in the HTML.

**Table 1.** Summary of U-Pb, $^{40}$Ar/$^{39}$Ar, and Fission Track Results[a]

| Sample | Elevation, m | U-Pb Zircon, Ma | $^{40}$Ar/$^{39}$Ar | | | Fission Track | |
|---|---|---|---|---|---|---|---|
| | | | Muscovite, Ma | Biotite, Ma | K-Feldspar, Ma | Apatite, Ma | Zircon, Ma |
| *Northern (Amaguaya) Transect* | | | | | | | |
| Yani granite | | | | | | | |
| RJG7 | 3042 | | 42.9 ± 1.1 | 40.7 ± 0.6 | 43.7 ± 4.5 | 8.6 ± 0.7 | |
| RJG8 | 3343 | 267–217 | 52.4 ± 1.3 | 44.6 ± 0.8 | | 10.5 ± 0.9 | |
| RJG9 | 3414 | | 84.0 ± 2.1 | 39.4 ± 0.6 | 42.1 ± 3.1 | 10.0 ± 0.9 | |
| RJG1 | 3805 | 273–218 | 55.0 ± 2.0 | 44.9 ± 0.7 | 34.6 ± 1.4 | 16.2 ± 1.3 | |
| 03RJG15 | 3976 | | 109.4 ± 4.9 | 132.5 ± 3.0 | 47.6 ± 3.1 | 15.4 ± 1.5 | |
| RJG2 | 4074 | | 99.4 ± 3.8 | 38.3 ± 0.7 | | 10.3 ± 0.9 | |
| RJG3 | 4335 | | | 47.5 ± 0.8 | | 17.9 ± 1.8 | |
| Illampu granite | | | | | | | |
| 03RJG16 | 4612 | 251–226 | 161.4 ± 3.9 | 55.2 ± 2.1 | | 14.3 ± 1.2 | |
| RJG14 | 4421 | | 148.3 ± 4.2 | 43.9 ± 0.8 | | | |
| RJG4 | 4714 | | 191.8 ± 3.8 | 74.5 ± 2.1 | | 10.4 ± 1.7 | |
| RJG5 | 5020 | | 149.2 ± 4.6 | 130.1 ± 4.7 | | 11.2 ± 3.7 | |
| RJG6 | 5363 | | 192.9 ± 3.9 | 107.2 ± 3.8 | | 18.2 ± 1.1 | |
| *Central (Rio Zongo) Transect* | | | | | | | |
| Huayna Potosí granite | | | | | | | |
| RZG19 | 5400 | | | 217.6 ± 3.5 | | 16.3 ± 1.0 | 151.0 ± 12.0 |
| RZG17 | 4360 | 241–218 | | | | | |
| Zongo granite | | | | | | | |
| RZG11 | 2840 | 263–227 | | | | | |
| *Southern (Quimsa Cruz) Transect* | | | | | | | |
| Quimsa Cruz granite (Mina Argentina) | | | | | | | |
| QCG8 | 3559 | | | 23.3 ± 0.4 | | | |
| QCG7 | 3900 | 25.65 ± 0.41 | | 23.4 ± 0.4 | | 6.8 ± 0.6 | |
| QCG6 | 4438 | | | 23.9 ± 0.8 | | 5.8 ± 0.5 | |
| Quimsa Cruz granite (Mina Viloco) | | | | | | | |
| QCG5 | 4830 | 26.02 ± 0.41 | | 23.9 ± 0.4 | | 15.5 ± 1.3 | |
| QCG4 | 5108 | | | 24.6 ± 0.4 | | 16.2 ± 2.4 | |
| *Eastern Altiplano Basin* | | | | | | | |
| Aranjuez Formation tuffs | | | | | | | |
| 03Taa01 | | | | 25.48 ± 0.40 | | | |
| 03Taa02 | | | | 26.69 ± 0.54 | | | |
| 03Taa03 | | | | 25.08 ± 0.54 | | | |
| 03Taa04 | | | | 27.40 ± 0.54 | | | |
| 03Taa05 | | | | 25.23 ± 0.42 | | | |
| 03Taa06 | | | | 33.13 ± 0.80 | | | |
| Salla Formation tuffs | | | | | | | |
| 03Tsal4 | | | | 28.00 ± 0.68 | | | |
| 03Tsal6 | | | | 24.59 ± 0.39 | | | |

[a]Errors reported at the 1$\sigma$ level. Most U-Pb values represent observed age range of noninherited zircon grains (see text); U-Pb ages for QCG7 and QCG5 are based on the weighted mean of noninherited zircon grains. The $^{40}$Ar/$^{39}$Ar ages are weighted mean ages. Fission track ages are pooled ages. See the auxiliary material for complete analytical results.

grains have high U contents (>1000 ppm) and low Th/U values (<0.1), signaling high susceptibility to Pb loss and/or metamorphic recrystallization. This possibility is supported by the fact that U-Pb analyses obtained from the Permo-Triassic granitoids tend to spread out over an age range of ~270–220 Ma (Table S1). For the conditions under which the analyses were undertaken, a homogeneous zircon population would be expected to exhibit a much smaller spread in U-Pb age (±2% or ±5 Ma 1$\sigma$ at 250 Ma). Because the observed age variability is much higher, we regard the possibility that Pb loss and/or metamorphic recrystallization induced the observed age spread as a real concern. Accordingly, for these samples we report the measured age range and refrain from making precise interpretations regarding crystallization age.

## 4.1. Quimsa Cruz Intrusive Complex

[33] The Quimsa Cruz intrusion is composed of two units. The main phase Mina Argentina (Mina Caracoles) body consists of granodiorite and monzogranite. A second phase situated to the SW is the Mina Viloco porphyritic monzogranite with K-feldspar megacrysts [*Miller*, 1988; *Miller and Harris*, 1989; *Kennan et al.*, 1995]. Seventeen of 18 zircon $^{206}$Pb/$^{238}$U ages from the Mina Argentina sample (QCG5) and 10 of 11 results from the Mina Viloco sample (QCG7) define distributions of late Oligocene crystallization ages that are comparable in analytical scatter (±3.5% and ±2.2% 1$\sigma$) to that expected from homogeneous samples based upon the reproducibility of standard analyses during the run (±2%). From these results we calculate

weighted mean ages of 26.2 ± 0.2 Ma (QCG5; Figure 5e) and 25.4 ± 0.2 Ma (QCG7; Figure 5f), respectively. Our results conflict with less precise data that suggested Eocene cooling for this pluton [*Kennan et al.*, 1995; *Lamb et al.*, 1997]. Moreover, we did not confirm a proposed older Permo-Triassic heritage [*Miller*, 1988; *Miller and Harris*, 1989; *Lamb and Hoke*, 1997]. The Mina Argentina sample yielded a discordant late Paleozoic grain while the Mina Viloco sample produced one discordant zircon with a $^{207}Pb/^{206}Pb$ age of 2656 ± 6 Ma. This Late Archean age matches older provinces of the Amazon craton to the east [e.g., *Santos et al.*, 2000] and could conceivably imply inheritance from cratonic rocks underthrust beneath the central Andean plateau [e.g., *Beck and Zandt*, 2002].

### 4.2. Illampu Granite

[34] Eight of 10 zircons analyzed from the Illampu granite (03RJG16) yield Late Permian to Late Triassic $^{206}Pb/^{238}U$ ages (251–226 Ma). Uranium concentrations are in excess of 1000 ppm with the highest U grain (3500 ppm) yielding a Th/U value of 0.004 that is typical of metamorphic recrystallization. We consider it possible that the Illampu granite was emplaced as early as ~250 Ma and that the younger ages reflect Pb loss and metamorphic recrystallization. Two Silurian U-Pb ages (~430 Ma) were also measured (Figure 5a) from low U grains (<500 ppm) with Th/U values typical of magmatic conditions (>0.1). These U-Pb results are similar in age to reset metamorphic crystalline basement in the Western Cordillera [*Wörner et al.*, 2000] and probably represent assimilated wall rock.

### 4.3. Yani Granite

[35] Results from the Yani granite (RJG1) are similar to those from the Illampu body in that 10 of 18 zircons define a range of $^{206}Pb/^{238}U$ ages between 273 and 218 Ma (Figure 5b). Similar to the Illampu Granite, some grains with high U and low Th/U content are present. However, relatively low U grains (<500 ppm) with magmatic Th/U (>0.1) values also occur in the youngest portion of the age distribution, at 230–218 Ma. Hence the implications of the results for determining the emplacement age of the Yani granite are ambiguous and more detailed work is required. Nevertheless, it seems clear that the granite was likely intruded during Permo-Triassic time. The remaining 8 zircons yield variably discordant U-Pb ages that appear to reflect assimilation of basement of early Paleozoic and Late Proterozoic age, similar to the Altiplano and Western Cordillera [*Lehmann*, 1978; *Wörner et al.*, 2000].

### 4.4. Huayna Potosí Granite

[36] Ten of 12 zircon $^{206}Pb/^{238}U$ ages measured from the Huayna Potosí granite (RZG17) define a range from 241 to 218 Ma (Figure 5c). Similar to the previous sample, some high U, low-Th/U analyses were obtained along with lower U analyses characterized by magmatic Th/U values. More detailed work is required to more rigorously assess the emplacement age of the Huayna Potosí granite. The two

older analyses are slightly discordant and appear to represent assimilated early Paleozoic basement.

### 4.5. Zongo Granite

[37] Eleven of 15 zircons measured from sample RZG11 from the Kuticucho phase of the Zongo granite [*McBride et al.*, 1987] define a range of $^{206}Pb/^{238}U$ ages from 263 to 227 Ma (Figure 5d). The combination of high U concentrations (typically $\gg$ 1000 ppm) and low Th/U values (generally <0.03) indicate a high probability that Pb loss and/or metamorphic recrystallization significantly affect the results. The remaining 4 analyses are variably discordant and appear to represent assimilated early Paleozoic and Late Proterozoic basement rocks.

## 5. The $^{40}Ar/^{39}Ar$ Thermochronology

[38] The $^{40}Ar/^{39}Ar$ step-heating analyses were carried out on 18 granite and 8 tuff samples (Table 1). A more detailed accounting of the methods employed and results obtained is provided in Table S2 (see auxiliary material). Uncertainties are reported at the $1\sigma$ level and include analytical errors and uncertainties in J factors.

[39] The new $^{40}Ar/^{39}Ar$ data help constrain cooling histories for the Cordillera Real granitoids and eruption ages for volcanic tuffs within the Cenozoic succession of the eastern Altiplano. Previous investigations of granites in the Cordillera Real and along strike in southern Peru identified complex thermal histories believed to have resulted from Eocene thrust-induced heating and subsequent cooling [*Evernden et al.*, 1977; *McBride et al.*, 1983, 1987; *Farrar et al.*, 1988; *Heinrich*, 1988; *Kontak et al.*, 1990; *Sandeman et al.*, 1995]. This interpreted tectonothermal episode of transient heating was considered to have produced anomalous relationships (i.e., biotites yielding older ages than corresponding muscovites [*McBride et al.*, 1987; *Farrar et al.*, 1988; *Kontak et al.*, 1990]). New $^{40}Ar/^{39}Ar$ results reveal a more straightforward pattern of mica and K-feldspar $^{40}Ar/^{39}Ar$ ages that can be interpreted as the product of exhumation-related cooling. Finally, while previous studies have dated volcanic horizons in the eastern Altiplano basin [e.g., *MacFadden et al.*, 1985; *Kay et al.*, 1998], the age of the oldest synorogenic fill remained poorly constrained. New $^{40}Ar/^{39}Ar$ biotite ages presented here indicate that the sediments were deposited several million years earlier than previously indicated.

### 5.1. Northern Transect

[40] The 12 granite samples along the northern transect yield $^{40}Ar/^{39}Ar$ total gas ages that become progressively younger with decreasing elevation. This overall relationship is similar to that determined in previous studies [e.g., *Farrar et al.*, 1988; *Kontak et al.*, 1990]. From SW to NE (5363 to 3042 m), muscovite ages decrease from 193 ± 4 to 43 ± 1 Ma. Similarly, biotite ages decrease from 133 ± 3 to 39 ± 1 Ma (Figure 6 and Table 1). Unfortunately, features exhibited by the age spectra indicate variable contamination with excess $^{40}Ar$ ($^{40}Ar_E$) [*Roddick et al.*, 1980; *Dallmeyer*
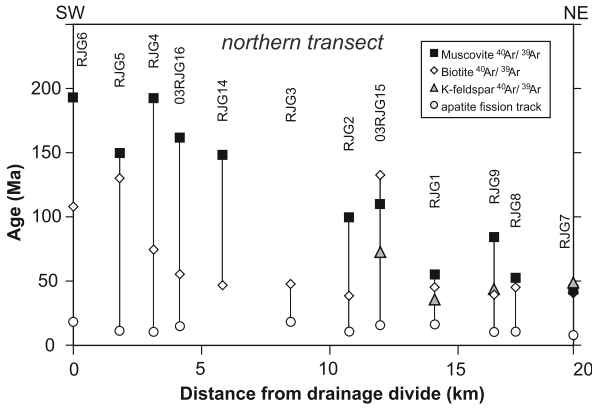
**Figure 6.** Age-distance plot showing $^{40}Ar/^{39}Ar$ muscovite, biotite, and K-feldspar results and apatite fission track (AFT) data for 12 samples along the northern transect. At this scale, the individual $1\sigma$ age errors are contained within the various geometric symbols.

*and Rivers*, 1983; *Zeitler and Fitz Gerald*, 1986; *Foster et al.*, 1990; *Baxter et al.*, 2002] (Figure 7). Results of isothermal duplicate and quadruplicate experiments in the initial heating steps for K-feldspar confirm retention of excess argon in the lower gas release portions for K-feldspars examined in this study. These materials yield saddle-shaped age spectra that indicate $^{40}Ar_E$ contamination affects both low- and high-temperature gas release (Figure 8) [e.g., *Harrison et al.*, 1994].

[41] In general, biotite $^{40}Ar/^{39}Ar$ age spectra exhibited less evidence of $^{40}Ar_E$ contamination at the lower elevation localities in the NE (i.e., below 4400 m elevation). These biotites yielded younger ages and flatter age spectra (Figure 7a) than biotites collected from above 4400 m in the SW (Figure 7b). Muscovite results exhibited similar patterns. For example, the youngest NE muscovite (RJG7) yields a flat age spectrum with little evidence of distur-

bance. In contrast, high-elevation muscovites from the SW yield saddle-shaped spectra (Figure 7c).

[42] Although $^{40}Ar_E$ contamination clearly limits our ability to carry out detailed interpretation of the $^{40}Ar/^{39}Ar$ data, several considerations suggest that the overall extent of contamination was not sufficient to preclude meaningful interpretation of the overall nature of the results. For example, none of the micas are so contaminated with $^{40}Ar_E$ that $^{40}Ar/^{39}Ar$ ages exceed corresponding U-Pb crystallization ages. Also, coexisting muscovite and biotite generally yield similar ages. In 10 of 11 cases, the muscovites were older than coexisting biotite, as expected from their high intrinsic Ar retentivity. This relationship contrasts with that reported for the Zongo-San Gabán region extending from the Cordillera Real ~450 km to the NW into southern Peru where biotites are apparently so contaminated with $^{40}Ar_E$ that their K-Ar ages commonly exceed those of coexisting muscovite [*McBride et al.*, 1987; *Farrar et al.*, 1988; *Kontak et al.*, 1990]. Finally, the lowest elevation sample along the transect yields highly correlated inverse isochrons for muscovite and biotite consistent with nearly atmospheric trapped argon (Table S2; see auxiliary material). Hence we believe that at least the topographically lowest samples yield geologically meaningful ages that constitute a robust record of Cenozoic cooling within the study region. For biotite, the younger ages (8 of 12 samples) fall between $38.3 \pm 0.7$ and $55.2 \pm 2.1$ Ma. The younger muscovite ages (3 of 11 samples) range from $42.9 \pm 1.1$ to $55.0 \pm 2.0$ Ma. As detailed below, the Eocene mica bulk closure ages can be explained by acceleration of denudation rates in the middle Eocene with continued high rates persisting into the Oligocene.

[43] To further quantify Cenozoic cooling for the northern transect, we also measured K-feldspar $^{40}Ar/^{39}Ar$ age spectra and interpreted the results using the multidiffusion domain (MDD) model [*Lovera et al.*, 1989, 1997, 2002; *Lee*, 1995; see also *Parsons et al.*, 1999]. Because the K-feldspar age spectra are seriously affected by $^{40}Ar_E$, we limited our modeling efforts to the least affected portion of
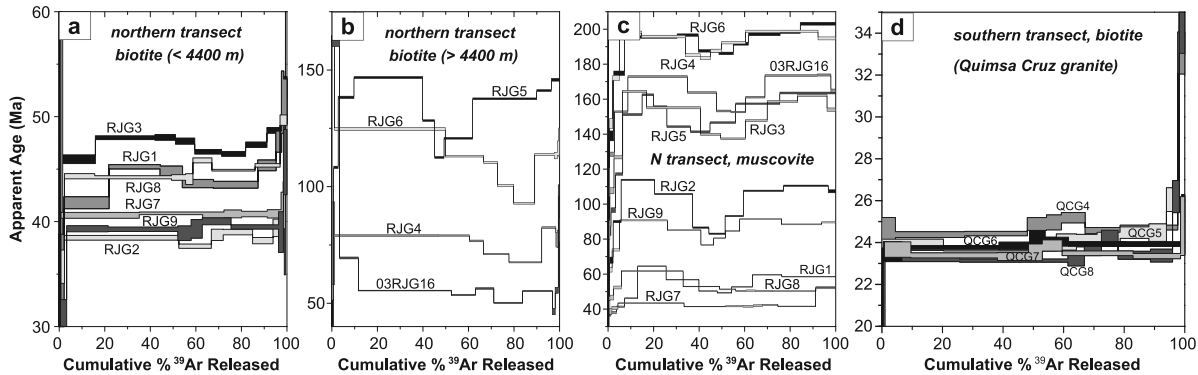


**Figure 7.** The $^{40}Ar/^{39}Ar$ age spectra for biotite and muscovite grains from granite samples of the northern and southern transects. Note variable scale on vertical (age) axes. (a) Northern transect biotite (<4400 m). (b) Northern transect biotite (>4400 m). (c) Northern transect muscovite. (d) Southern transect biotite.
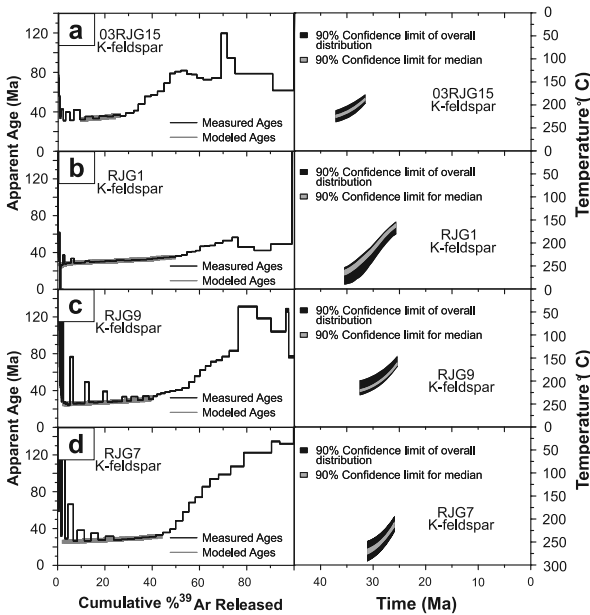
**Figure 8.** (left) The $^{40}$Ar/$^{39}$Ar age spectra and (right) multidomain diffusion (MDD) modeling results for K-feldspar grains from Yani granite samples of the northern transect. (a) Sample 03RJG15. (b) Sample RJG1. (c) Sample RJG9. (d) Sample RJG7.

the age spectra (i.e., intermediate release steps [see *Zeitler and Fitz Gerald*, 1986; *Lovera et al.*, 2002]). MDD modeling of four K-feldspars from the Yani granite at lower elevations of the northern transect (Figure 8) constrain the mid-Cenozoic thermal histories and help link the higher temperature $^{40}$Ar/$^{39}$Ar mica results to the apatite fission track results discussed below. The MDD model results (Figure 8) demonstrate 8–12°C/Ma cooling between about 38 and 26 Ma with average cooling rates generally increasing with decreasing elevation from SW to NE.

### 5.2. Southern Transect

[44] Biotite $^{40}$Ar/$^{39}$Ar analyses from five Quimsa Cruz samples along a vertical interval of ~1550 m (Figures 3 and 7d) yield late Oligocene–earliest Miocene cooling ages ranging from 24.6 ± 0.4 to 23.3 ± 0.4 Ma (Table 1). The samples produce relatively flat age spectra (Figure 7d) and become younger with decreasing elevation to the NE. The fact that the biotite $^{40}$Ar/$^{39}$Ar results are slightly younger than the ~26 Ma U-Pb zircon crystallization age measured from the Quimsa Cruz granite is consistent with a depth of emplacement of >4 km [see also *Miller*, 1988; *Lamb and Hoke*, 1997].

### 5.3. Depositional Age Constraints for the Altiplano Basin

[45] Biotite $^{40}$Ar/$^{39}$Ar results are reported for 8 volcanic tuffs in the Cenozoic succession of the eastern Altiplano (Figure 9 and Table 1). A discontinuous belt of exposed

basin fill occurs between 16 and 17.5°S, including the Peñas and Aranjuez formations in the north and the Luribay and Salla formations in the south (Figure 1b) [*Martinez*, 1980; *Geobol*, 1993, 1995; *Suárez and Diaz*, 1996].

[46] The deposits are 500–1500 m thick, but only the upper levels of the southern exposures have been studied in detail, where previous fission track, $^{40}$Ar/$^{39}$Ar, and magnetostratigraphic studies have revealed Oligocene deposition of the Salla Formation from 29.4 to 25.5 Ma [*MacFadden et al.*, 1985; *McRae*, 1990; *Kay et al.*, 1998]. New results for tuffs in the lower to intermediate levels include six tuffs of the Aranjuez Formation ranging from 33.1 ± 0.8 to 25.2 ± 0.4 Ma (Table 1). Two additional tuffs from the Salla Formation yield ages of 28.0 ± 0.7 and 24.6 ± 0.4 Ma. These results demonstrate that sediment accumulation had already commenced in the eastern Altiplano by the Eocene-Oligocene boundary, earlier than commonly envisioned [e.g., *Sempere et al.*, 1990].

## 6. Fission Track Thermochronology

[47] Fission track analysis was employed to further evaluate the low-temperature (<120°C) cooling history of the Cordillera Real. Apatite fission track (AFT) data help constrain the time at which rocks were exhumed above ~4 km depth (110–120°C), assuming a steady geothermal gradient. Moreover, their track length distributions can be modeled to constrain low-temperature (~60–120°C) thermal histories [*Laslett et al.*, 1987; *Lutz and Omar*, 1991; *Willett*, 1997; *Ketcham et al.*, 2000]. The new results build upon those of previous studies, notably *Benjamin et al.* [1987], who presented AFT and zircon fission track (ZFT) results along the central (Rio Zongo) transect. Additional fission track data have also been presented within the context of several other studies [*Crough*, 1983; *Heinrich*, 1988; *Safran*, 1998]. The previous results have given rise to conflicting interpretations regarding the onset and rates of cooling in the region [*Benjamin*, 1986; *Benjamin et al.*, 1987; *Masek et al.*, 1994; *Lamb and Hoke*, 1997; *Safran*, 1998; *Moore and England*, 2001; *Anders et al.*, 2002].

[48] Seventeen fission track analyses were performed on 16 granite samples, including 11 AFT results for the northern transect, 4 AFT results for the southern transect,
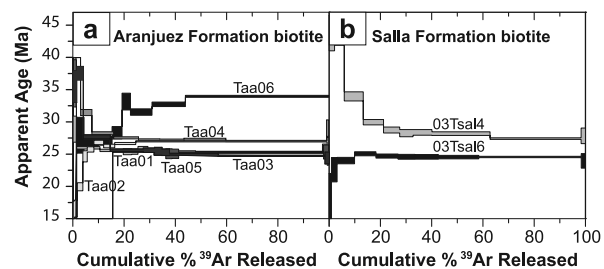


**Figure 9.** The $^{40}$Ar/$^{39}$Ar age spectra for biotite grains from volcanic tuffs of the eastern Altiplano basin. (a) Results for six tuff samples from the Aranjuez Formation. (b) Results for two tuff samples from the Salla Formation.

and AFT and ZFT results for a single sample from the central transect. AFT ages range from 18.2 to 5.8 Ma, with significant age overlap among the transects (Figure 6 and Table 1). Ages are reported as pooled values with $1\sigma$ errors. Complete results are reported in Table S3 (see auxiliary material).

[49] Modeling of the new AFT data yields results consistent with those obtained from higher-temperature $^{40}Ar/^{39}Ar$ thermal history data (i.e., acceleration of denudation rates in the middle Eocene with continued high rates persisting into the Oligocene). Similar to $^{40}Ar/^{39}Ar$ data, the fission track results show progressively younger ages from SW to NE, from high to low elevation (Figure 6). For the northern transect, the oldest and youngest AFT ages of 18.2 and 8.6 Ma are from the highest and lowest (5363 and 3042 m) samples, respectively. AFT ages for the southern transect generally correlate with elevation, from 16.2 to 5.8 Ma between 5108 and 3900 m. The ZFT age of 151 Ma for the central transect provides a critical data point for the Huayna Potosí granite at 5400 m, clarifying previous interpretations of *Benjamin et al.* [1987]. A correlation between AFT age and elevation throughout the Cordillera Real suggests a simple record of exhumation-induced cooling. However, a few samples depart slightly from this trend, suggestive of locally more complex histories possibly related to a variable thermal structure at shallow depth, as dictated by topographic relief.

### 6.1. Northern Transect

[50] AFT analyses were performed on 11 of 12 samples from the northern transect. The AFT results (Table 1) show Miocene cooling, with ages ranging from $18.2 \pm 1.1$ Ma for the highest SW sample to $8.6 \pm 0.7$ Ma for the lowest NE sample (Figure 6). Mean track lengths vary from $11.83 \pm 0.28$ to $14.06 \pm 0.20$ $\mu$m, with standard deviations of generally $1.5-2.7$ $\mu$m. AFT ages are generally older at higher elevation although a few exceptions to this trend are interspersed along the transect (Table 1). The younger samples generally have longer mean track lengths and overall more restricted length distributions (Table 1) indicating more rapid cooling [*Green*, 1986; *Fitzgerald*, 1994].

### 6.2. Southern Transect

[51] AFT analyses of the four Quimsa Cruz samples yield ages ranging from $16.2 \pm 2.4$ to $5.8 \pm 0.5$ Ma (Table 1). The younger samples are located at lower elevations in the NE while the older ages are generally from the highest part of the transect in the SW. Relative to the northern transect, the mean track lengths tend to be slightly longer, ranging from $13.19 \pm 0.24$ to $13.75 \pm 0.26$ $\mu$m (Table 1). However, average track length distributions are comparable to slightly broader, with standard deviations of $2.19-2.66$ $\mu$m, suggesting potentially more complex thermal histories [e.g., *Fitzgerald and Gleadow*, 1988]. When considered together with the $^{40}Ar/^{39}Ar$ biotite results, the fission track data clearly support late Oligocene through late Miocene slow exhumation of the Quimsa Cruz granite. Although the data set is limited, the younger AFT ages are consistent with a phase of accelerated denudation beginning at ~6 Ma.

### 6.3. Modeling of AFT Results

[52] Permissible AFT cooling histories were constrained by the measured track length distributions and kinetic parameters derived from etched track pit diameters ($D_{par}$ values) [*Carleson et al.*, 1999; *Donelick et al.*, 1999; *Ketcham et al.*, 1999, 2000]. Measured track lengths have been corrected using a C axis projection [*Donelick et al.*, 1999] and each sample was modeled assuming a single kinetic population, consistent with the observed narrow range in $D_{par}$ values ($1.51-1.64$ $\mu$m). Confidence limits of the cooling paths were produced using a Monte Carlo search algorithm, yielding an "acceptable fit" envelope (statistical probability value = 0.05), and a "good fit" envelope (statistical probability value = 0.5) [*Ketcham et al.*, 2000].

[53] AFT modeling for the northern transect reveals nearly linear, <120°C time-temperature paths indicative of uniform rapid cooling from late Miocene onward (Figure 10a). In contrast, older samples display variable cooling histories. Several older samples (notably 03RJG16 and RJG3) suggest slower cooling during the early to middle Miocene followed by rapid late Miocene cooling (Figure 10b). The remaining older samples (RJG6, 03RJG15, and RJG1) exhibit approximately linear trends suggesting uniform cooling from late Oligocene–early Miocene to Pliocene time.

[54] Approximate cooling rates were estimated for modeled "good fit" cooling envelopes between 110 and 60°C. The younger, 8.6–11.9 Ma samples (Figure 10a) yield cooling of 7–12°C/Myr between ~10 and ~6 Ma. The older samples (Figure 10b) exhibit cooling of generally <5°C/Myr between ~23 and ~8 Ma. For the southern transect, AFT thermal models indicate cooling of <5–11°C/Myr from ~19 to ~9 Ma, with more rapid late Miocene cooling of <5–20°C/Myr. Overall, the AFT ages and model results (Figure 10) indicate rapid cooling <120°C during late Miocene to Pliocene time, with some samples suggesting earlier slower cooling during early to middle Miocene time. Moreover, the results are quite consistent with the K-feldspar $^{40}Ar/^{39}Ar$ results in that they indicate continued rapid cooling during Eocene-Oligocene time.

## 7. Cenozoic Exhumation of the Cordillera Real

### 7.1. Integrated Thermal Histories

[55] Thermochronologic results help constrain the cooling history of the Cordillera Real. Composite thermal histories were constructed using $^{40}Ar/^{39}Ar$ results and relevant closure temperatures for muscovite (400–345°C) and biotite (325–280°C) [*McDougall and Harrison*, 1999], MDD modeling of K-feldspar $^{40}Ar/^{39}Ar$ results (250–150°C) [*Lovera et al.*, 1989], and modeling of apatite fission track length distributions (120–60°C) [*Ketcham et al.*, 2000].

[56] Four samples from the northern transect (03RJG15, RJG1, RJG9, and RJG7) were targeted on the basis of (1) lower excess argon retention, suggesting more reliable, longer duration MDD histories, (2) lower uncertainties for
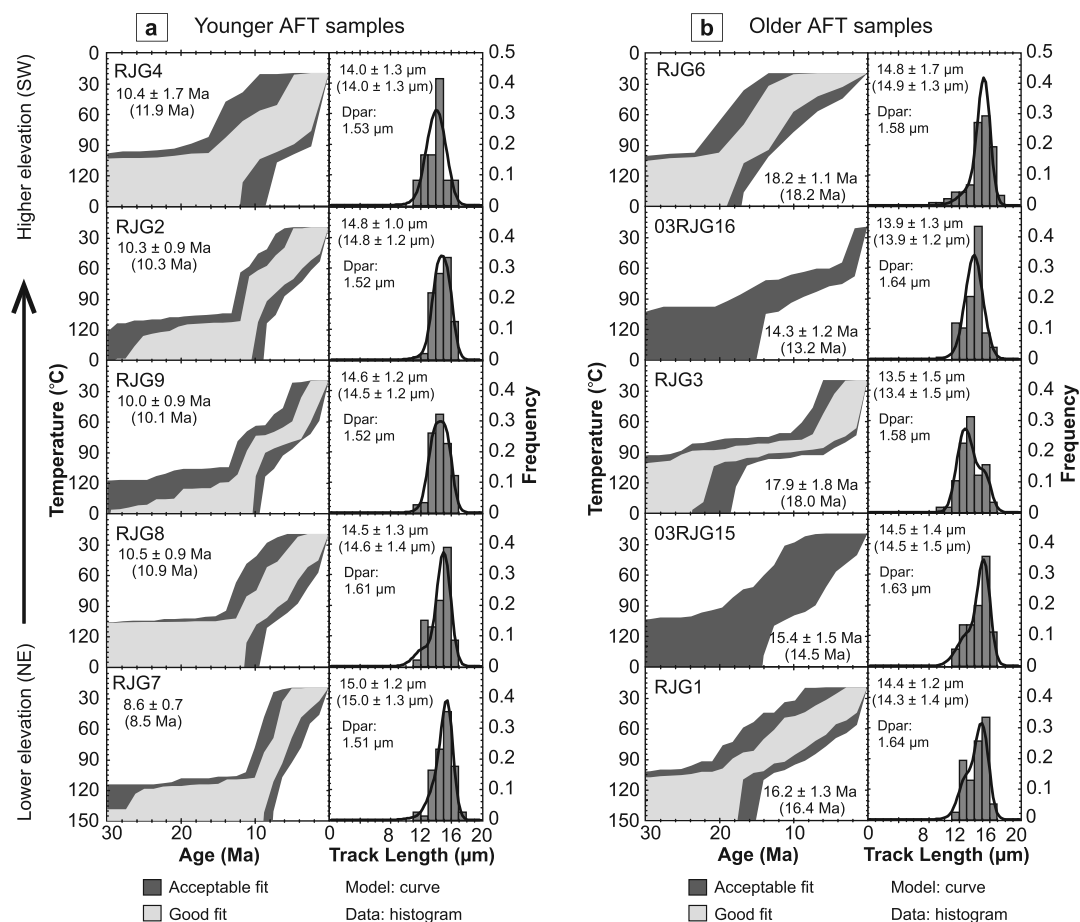
**Figure 10.** Apatite fission track (AFT) (left) thermal modeling results and (right) track length data for (a) younger samples and (b) older samples. Each AFT model shows the calculated time-temperature path, pooled age, and modeled age (in parentheses). Each track length plot shows the track length distribution (histogram), modeled distribution (curve), observed mean track length, and modeled mean track length (in parentheses). All reported track lengths represent corrected values using a C axis projection [*Donelick et al.*, 1999].

AFT modeling results, and (3) the internal consistency afforded by samples from the same rock unit, the Yani granite. The MDD and AFT cooling histories are plotted in time-temperature space, along with the $^{40}Ar/^{39}Ar$ mica ages (Figure 11). High-temperature portions of the AFT models were constrained by requiring the composite thermal histories to fit the lowest, well-defined temperature envelope of the MDD models.

[57] Higher elevation samples in the SW (03RJG15 and RJG1) exhibit protracted histories that extend back to Cretaceous–early Cenozoic time. Their cooling paths show pronounced slope breaks in time-temperature space indicative of an onset of rapid cooling during the middle to late Eocene (40–35 Ma; Figures 11a–11b). The highest sample shows uniform cooling since ~37 Ma at 6°C/Myr while the other suggests a slight reduction in cooling rate at ~26 Ma, from 10 to 5°C/Myr.

[58] The topographically lower NE samples (RJG9 and RJG7) record more abbreviated histories that commenced at 45–40 Ma. Steeper segments of the cooling paths indicate two phases of rapid cooling: an initial middle Eocene–Oligocene phase that was underway by ~40 Ma and persisted until ~26 Ma and a second phase from late Miocene onward (Figures 11c–11d). The cooling paths reveal initial rapid cooling between about 43 and 26 Ma at 11°C/Myr and later rapid cooling at 9–16°C/Myr from ~11 Ma onward. A period of nearly isothermal conditions appears to separate the two phases of rapid cooling. This episode of diminished cooling is further supported by AFT model results for additional samples, notably RJG3 (Figure 10b), which indicates <1.0–2.0°C/Myr cooling from 22 to 8 Ma.

[59] In summary, the integrated cooling histories uniformly identify a middle Eocene inception of rapid cooling.
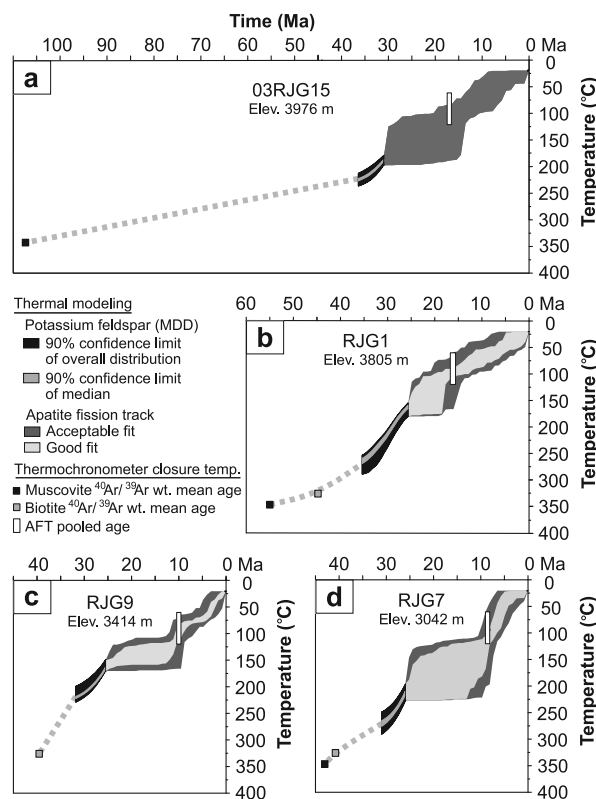
**Figure 11.** Composite thermal modeling results (combined $^{40}Ar/^{39}Ar$ MDD modeling and AFT thermal modeling) for four granite samples from the northern transect. (a) Sample 03RJG15. (b) Sample RJG1. (c) Sample RJG9. (d) Sample RJG7.

This phase of rapid cooling (11°C/Myr) persisted from 45–40 to ~26 Ma. Lower-elevation samples further constrain a period of reduced cooling from ~26 to ~11 Ma (0–2°C/Myr) followed by rapid cooling (9–16°C/Myr) from ~11 Ma onward.

## 7.2. Age-Elevation Relationships

[60] Examination of the variation of mica $^{40}Ar/^{39}Ar$ ages as a function of elevation further constrains the higher temperature cooling history of the Cordillera Real. Provided an increase in cooling rate, samples will define a broad age range at high elevation that narrows with decreasing elevation. These age patterns are produced by the intersection of present-day topography and paleodepth as manifested by the exhumed partial retention zone for Ar in the micas. When not obscured by $^{40}Ar_E$ contamination, the onset of rapid cooling will be marked as an abrupt inflection in a plot of age vs. elevation that defines the lower limit of the partial retention zone (Figure 12a) [*Fitzgerald et al.*, 1995].
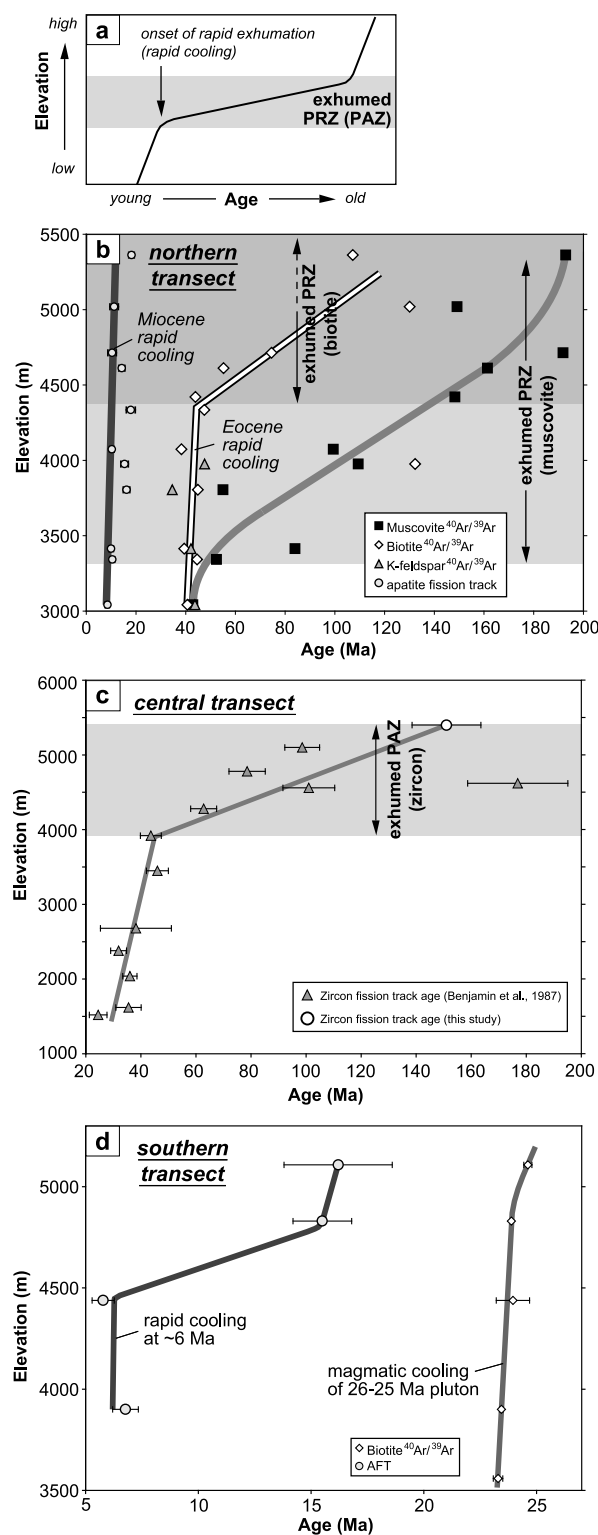
[61] This predicted relationship is observed within the Cordillera Real in spite of complications related to $^{40}Ar_E$ contamination at high elevation. The $^{40}Ar/^{39}Ar$ age differences for 11 muscovite-biotite pairs along the northern

transect become systematically smaller (from ~86 to ~2 Myr) from high to low elevations. This relationship suggests the low-elevation micas were sufficiently deep that they were completely open with respect to Ar retention and closed only as a result of initial rapid cooling during the middle Eocene (Figure 6). We interpret the transition from distributed biotite ages (130.1–55.2 Ma) to clustered ages (47.5–38.3 Ma) below ~4500 m elevation as indicating the onset of rapid cooling at 45–40 Ma (Figure 12b). Assuming a steady 30°C/km geothermal gradient [*Benjamin et al.*, 1987; *Henry and Pollack*, 1988], the biotite results indicate that the average cooling rate increased at 45–40 Ma from <5 to 10°C/Myr. $^{40}Ar/^{39}Ar$ weighted mean ages for biotite, muscovite, and K-feldspar from the lowest sample (RJG7) are nearly identical at 44–40 Ma (Figure 6 and Table 1), further supporting rapid cooling at this time.

[62] On an age-elevation plot, the broad distribution of muscovite cooling ages (Figure 12b) reflects relatively slow cooling at <5°C/Myr prior to middle Eocene time. An inflection in the trend of the data suggests that samples above ~3300 m resided in the muscovite partial retention zone prior to ~45 Ma. A similar inflection in the biotite data suggests that an exhumed partial retention zone for biotite is represented by samples above ~4400 m (Figure 12b). These data require that the samples resided in a narrow zone at 9–11.5 km depth prior to ~45 Ma, given the assumptions of closure temperature and geothermal gradient (Figure 11a). This estimate is in agreement with the reported ~10–15 km granite emplacement depth (3–5 kbar) [*McBride et al.*, 1983; *Heinrich*, 1988].

[63] A middle Eocene inception of rapid cooling is consistent with ZFT data for the central transect [*Benjamin et al.*, 1987] (Figure 12c). *Benjamin et al.* [1987] speculated that their oldest (176.9–62.8 Ma), highest elevation (5100–3900 m) samples cooled within the ZFT partial annealing zone prior to more rapid cooling at ~45 Ma. A new ZFT analysis of a sample from 5400 m elevation (Table 1), ~300 m above their highest sample, supports this interpretation. The data define a trend from widely distributed ZFT ages (roughly 177–63 Ma) at higher elevations to a narrow distribution of ages (mostly 45–32 Ma) below ~3900 m (Figure 12c). In addition, the younger ZFT ages of 36.0–31.9 Ma [*Benjamin et al.*, 1987] are similar to the youngest K-feldspar $^{40}Ar/^{39}Ar$ age of 34.6 ± 1.4 Ma for the northern transect (Table 1). These comparable ages, despite the disparity in closure temperatures, suggest that rapid cooling continued during late Eocene to Oligocene time. Moreover, the ZFT and $^{40}Ar/^{39}Ar$ mica data support the MDD and composite modeling results (Figures 8 and 11) indicating initial rapid cooling at 45–40 Ma.

[64] On an age-elevation plot, AFT data for the northern transect define a steep, nearly linear trend suggesting uniform rapid cooling was underway by about 10 Ma (Figure 12b). The absence of more broadly distributed data at higher elevations suggests that the partial annealing zone has been removed by erosion. Modest AFT age variations reveal that some anomalous older samples locally contradict the trend of increasing age at higher elevations (Figure 12b), as evidenced in a NE-SW profile (Figure 6). Several

**Figure 12.** (a) Schematic age-elevation plot of idealized distribution of ages associated with an exhumed partial retention/annealing zone (PRZ/PAZ) [after *Fitzgerald et al.*, 1995]. Thermochronometer sample age-elevation plots of $^{40}$Ar/$^{39}$Ar muscovite, biotite, and K-feldspar weighted mean ages, apatite fission track (AFT) pooled ages, and zircon fission track (ZFT) pooled ages for the (b) northern transect, (c) central transect, and (d) southern transect. The shaded lines represent the approximate age-elevation trends for the various thermochronometers.
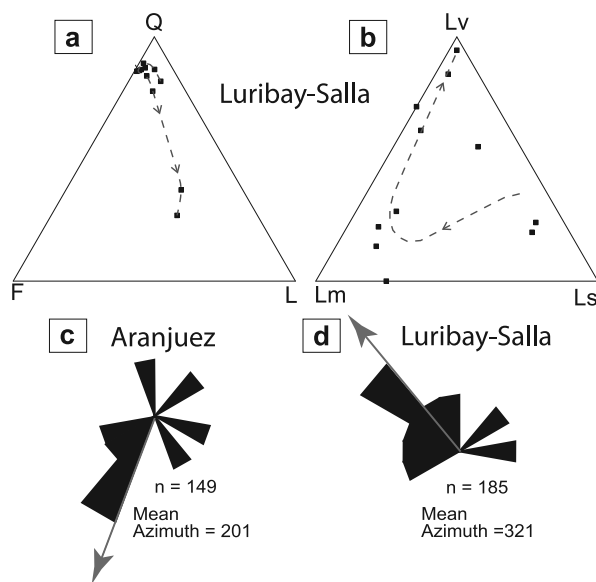
mechanisms may explain older samples interspersed with younger samples. First, postcooling displacement along faults could account for the age contradictions. However, the older ages generally occur in hanging wall settings, inconsistent with regional thrust faulting [*Pareja et al.*, 1978; *Martinez*, 1980; *McQuarrie*, 2002]. Second, because the 110–120°C isotherm is sensitive to topography at small wavelengths [e.g., *Stüwe et al.*, 1994], particularly in the high-relief regions such as the Cordillera Real [*Safran*, 1998], topographic effects on the former geothermal gradient may produce the necessary age variations. Third, the age discrepancies may be explained by compositional differences in apatite, as reflected by $D_{par}$ (etch pit diameter) values, which affect the closure temperature of individual samples [*Carleson et al.*, 1999]. Despite the narrow range of $D_{par}$ values (1.51–1.64 $\mu$m), there is a positive relationship between higher $D_{par}$ values (>1.60 $\mu$m) and older ages (Figure 10). We tentatively attribute the anomalous older AFT ages to the combined effects of topography and compositional variations.

[65] For the southern transect, the cooling history is constrained by limited $^{40}$Ar/$^{39}$Ar biotite and AFT results. On an age-elevation plot, the biotite ages reveal a steep, nearly linear trend at about 25–23 Ma (Figure 12d). Because U-Pb zircon ages reveal a ~26 Ma crystallization age for the Quimsa Cruz granite, the biotite suggest that modest rates of erosional denudation from >4 km depth accompanied pluton emplacement. AFT age data from four Quimsa Cruz samples define a stair step curve with an inflection suggestive of an increase in cooling rate at ~6 Ma (Figure 12d).

### 7.3. Eastern Altiplano Sedimentation

[66] The thermal record of exhumation is compatible with the sedimentation record of the eastern Altiplano. $^{40}$Ar/$^{39}$Ar ages of 8 tuffs (Figure 9 and Table 1) within the Cenozoic succession help define the age of basin fill at 16–17.5°S, including the Peñas, Aranjuez, Luribay, and Salla formations (Figure 1b) [*Martinez*, 1980; *MacFadden et al.*, 1985; *McRae*, 1990; *Sempere et al.*, 1990; *Geobol*, 1993, 1995; *Suárez and Diaz*, 1996; *Lamb and Hoke*, 1997; *Kay et al.*, 1998; *McQuarrie and DeCelles*, 2001]. The age data reveal deposition spanning the Oligocene, from 33.1 to 24.6 Ma.

[67] Provenance data (Figure 13) for these deposits reveal the composition of source areas and the sediment transport pathways. Sandstone petrographic analyses consisted of point counts (450 grains per thin section) of 11 samples

**Figure 13.** Provenance data for basin fill of the eastern Altiplano basin. (a) Quartz-feldspar-lithic fragments (Q-F-L) and (b) lithic volcanic-metamorphic-sedimentary fragments (Lv-Lm-Ls) ternary diagrams showing data and upsection trends (dashed arrows) for the Luribay-Salla succession. Paleocurrent rose diagrams and vector means for the (c) Aranjuez Formation and (d) Luribay-Salla succession.

from a ∼200 m stratigraphic interval in the Luribay Formation to middle Salla Formation. A modified Gazzi-Dickinson method of point counting was employed [*Ingersoll et al.*, 1984] and complete results are presented in Table S4 (see auxiliary material). Recalculated detrital modes are plotted in ternary diagrams depicting proportions of Q-F-L (quartz-feldspar-lithic fragments; Figure 13a) and Lv-Lm-Ls (lithic volcanic-metamorphic-sedimentary fragments; Figure 13b). Both diagrams show upsection variations in detrital composition. The Q-F-L plot displays a minor decrease followed by a dramatic increase in lithic fragments (Figure 13a). The Lv-Lm-Ls plot depicts an upsection shift from sedimentary to metamorphic fragments followed by a huge increase in the proportion of volcanic fragments (Figure 13b). Quartz, sedimentary, and metamorphic fragments are consistent with derivation from Paleozoic clastic sedimentary and metasedimentary rocks of the Eastern Cordillera. The Luribay-Salla sandstones generally contain a greater proportion of lithic fragments, particularly volcanic fragments, relative to previous Altiplano studies [*Horton et al.*, 2002], possibly related to closer proximity to sediment sources. In any case, the increased proportion of volcanic detritus is considered a record of increasing volcanism in the Cordillera Real, likely associated with emplacement of the Quimsa Cruz granite.

[68] Over 330 paleocurrent indicators were measured, including trough axes and trough limbs. Paleocurrent data for the Aranjuez and Luribay-Salla localities indicate trans-

port to the SSW and NW, respectively (Figures 13c and 13d). Similar to the compositional data, these dispersal patterns are compatible with derivation from the neighboring Cordillera Real.

[69] Structural relationships shed further light on Cenozoic basin evolution. Discontinuous exposures of the Peñas, Aranjuez, and Luribay-Salla formations aligned parallel to the Cordillera Real (Figure 1b) share similar ages, provenance, facies, and unconformable basal contacts on steeply dipping Silurian-Devonian strata. Growth strata within the Luribay Formation and lower levels of the 29.4–25.5 Ma Salla Formation indicate syndepositional activity along SW directed fold-thrust structures prior to ∼28 Ma [*Gillis et al.*, 2004]. Growth geometries are not observed in the subhorizontal strata of the upper succession, indicating late Oligocene cessation of upper crustal deformation in the region.

[70] The compositional and paleocurrent analyses demonstrate that the Cordillera Real was an active sediment source during early evolution of the eastern Altiplano basin. $^{40}Ar/^{39}Ar$ age data and structural relationships indicate that deposition was occurring from about 33 to 25 Ma, largely coeval with SW directed thrusting, in agreement with rapid Oligocene exhumation identified by thermochronologic data. These relationships indicate that crustal shortening, unroofing and rapid cooling were synchronous along the eastern margin of the central Andean plateau, suggesting that crustal shortening was a principal cause of exhumation in the early orogenic history.

## 8. Discussion

[71] Thermochronologic data help determine the history of exhumation-related cooling in the Cordillera Real, but a significant challenge lies in interpretation of the deformation history associated with this thermal record. In considering alternative tectonics models for the eastern flank of the central Andean plateau, several observations must be addressed.

### 8.1. Kinematics

[72] Structural data and crosscutting relationships restrict the magnitude and timing of shortening on upper crustal structures. Most notable is the limited displacement (<2–5 km) accommodated by most thrusts, suggesting 20 km of minimum NE-SW shortening (∼35% net strain) across the Cordillera Real (Figure 4). No evidence exists for near-surface large-magnitude thrusts. Nevertheless, the range exposes some of the deepest structural levels in Bolivia, implying a larger structure at depth near the Eastern Cordillera–Altiplano boundary [e.g., *Dorbath et al.*, 1993; *McQuarrie*, 2002].

[73] In terms of kinematics, upper crustal deformation postdated Permo-Triassic magmatism and early Paleocene deposition of the El Molino Formation (Figure 1b) [*Lamb and Hoke*, 1997; *DeCelles and Horton*, 2003; *Horton*, 2005]. Tighter age constraints are provided by growth strata indicating SW directed thrusting synchronous with Oligocene, and possibly late Eocene, sedimentation [*Gillis et al.*,
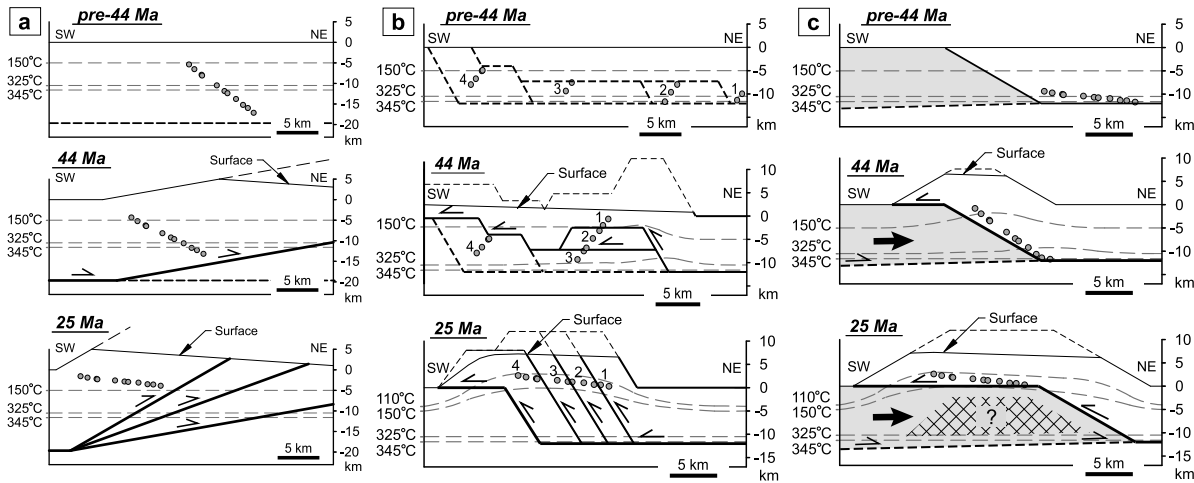
**Figure 14.** Alternative schematic models for the tectonic evolution of the Cordillera Real, depicting the Eocene-Oligocene history of the 11 samples (circles) of the northern transect at three stages: pre-44 Ma; 44 Ma; and 25 Ma. (a) Large-scale, down-to-SW tilting of the Cordillera Real due to motion along NE directed thrust structures. (b) SW directed thrusting linked to an in-sequence duplex system defined by four thrust sheets (1–4). (c) SW directed transport of a thick thrust sheet over a NE dipping ramp during tectonic wedging. Hatchures represent zone of possible duplexing.

2004]. $^{40}$Ar/$^{39}$Ar tuff ages (Figure 9 and Table 1) and sediment provenance information (Figure 13) suggest that deformation and surface uplift were in progress along the eastern flank of the central Andean plateau between 33 and 25 Ma. For younger age constraints, crosscutting relationships and U-Pb ages (Figures 3 and 5 and Table 1) show that fold-thrust deformation predated ∼26 Ma emplacement of the Quimsa Cruz granite [*Evernden et al.*, 1977; *Lamb and Hoke*, 1997]. Although it is widely accepted that upper crustal shortening in the Eastern Cordillera had ceased by ∼10 Ma, on the basis of the extensive San Juan del Oro surface [*Gubbels et al.*, 1993; *Kennan et al.*, 1997], intermontane basins throughout the Eastern Cordillera suggest that major upper crustal shortening was complete by latest Oligocene to earliest Miocene time [*Horton*, 2005]. With the emergence of improved timing constraints for the Cordillera Real and broader Eastern Cordillera of Bolivia, it is clear that Paleogene deformation is integral to the evolution of the central Andean plateau [e.g., *Horton et al.*, 2001; *DeCelles and Horton*, 2003; *Horton*, 2005; *McQuarrie et al.*, 2005a], in contrast to many studies that consider shortening to be younger than ∼25 Ma [*Isacks*, 1988; *Gubbels et al.*, 1993; *Allmendinger et al.*, 1997; *Kley and Monaldi*, 1998; *Gregory-Wodzicki*, 2000]. The observed map relationships suggest limited upper crustal deformation after ∼25 Ma, but do not rule out the possibility of Neogene passive transport of upper crustal material above deeper structures.

## 8.2. Cooling History

[74] In addition to structural constraints, a viable model must also explain thermochronologic results. $^{40}$Ar/$^{39}$Ar mica ages and multidomain diffusion (MDD) modeling of K-feldspar results demonstrate a middle Eocene initiation of rapid cooling at 45–40 Ma, consistent with the previous zircon fission track (ZFT) results of *Benjamin et al.* [1987], as supplemented by a single new ZFT analysis (Figure 12c). Thermal modeling of $^{40}$Ar/$^{39}$Ar and AFT results suggest that initial rapid cooling continued through the Oligocene to ∼26 Ma, followed by a period of slower cooling, then renewed rapid cooling commencing at ∼11 Ma (Figure 11). The $^{40}$Ar/$^{39}$Ar data display a pronounced and systematic decrease in muscovite and biotite ages from SW to NE (Figure 6), consistent with a northeastward progression of exhumation. $^{40}$Ar/$^{39}$Ar data suggest that all but the lowest-elevation sample cooled within the muscovite partial retention zone, and the 4 highest samples cooled within the biotite partial retention zone, requiring residence at ∼280–345°C prior to ∼45 Ma (Figure 12b). Given the assumptions of closure temperature and steady geothermal gradient, an estimated 9–11.5 km of total exhumation has occurred since 45–40 Ma, with ∼3.5 km of that since ∼11 Ma. These values are consistent with inferred ∼10–15 km granite emplacement depths [*McBride et al.*, 1983; *Heinrich*, 1988; *Miller*, 1988]) and further suggest that the middle Eocene–late Oligocene phase of rapid cooling accounts for most of the exhumation.

## 8.3. Tectonic Exhumation Models

[75] Several kinematic scenarios are capable of linking the histories of deformation and early exhumation along the eastern flank of the central Andean plateau. One possibility involves large-scale, southwestward tilting of the Cordillera Real in the backlimb of a belt of NE directed (10–30°SW dipping), crustal-scale thrusts (Figure 14a) [e.g., *Heinrich*, 1988; *Sheffels*, 1990; *Baby et al.*, 1997]. This tilting would produce the observed systematic decrease in cooling ages from SW to NE, and satisfy the observed low magnitudes of

slip along mapped faults. However, restoration of the sample transect to its predeformational state, by untilting the samples $10-30°$, would require the samples to have been originally arrayed over a $6-13$ km vertical extent (Figure 14a). Such a configuration is at odds with the paired muscovite-biotite $^{40}Ar/^{39}Ar$ ages requiring that most samples originally resided within a narrow temperature window at $9-11.5$ km depth.

[76] A second possibility is that mapped SW directed thrusts in the Altiplano at the SW front of the central Andean backthrust belt (Figure 1b) represent a system of high-magnitude thrusts that merge at depth to the NE into a regional décollement horizon (Figure 14b). If this large-magnitude structural system involved a duplex in Ordovician and older rocks [e.g., *McQuarrie et al.*, 2005b], it could produce substantial exhumation. In this model, rocks originally at $5-11$ km depth are carried up a system of ramps at different stages during in-sequence thrusting from NE to SW. Although this scenario satisfies the estimated total exhumation for some samples, it is not consistent with the northeastward decrease in $^{40}Ar/^{39}Ar$ cooling ages and the requirement that all samples originated at $9-11.5$ km depth.

[77] A third model similarly involves transport of a thick thrust sheet over a large NE dipping ramp (Figure 14c). This geometry is consistent with limited slip along most faults, but invokes a single large-magnitude, SW directed structure that has not been identified. Nevertheless, several candidates exist, including a seismically imaged crustal-scale boundary between the Altiplano and Eastern Cordillera [*Dorbath et al.*, 1993] that may correspond to the Cordillera Real Fault Zone [*Martinez*, 1980], a poorly defined structure apparently marking the SW margin of the granite belt (Figure 1b). Because of the lack of cutoffs, it is conceivable that a structure along the SW flank of the granite belt accommodated significant displacement. Alternatively, a large-magnitude structure may be covered by young basin fill or may have fed slip into the Coniri and Huarina faults (Figure 1b) at the SW front of the central Andean backthrust belt [*Martinez*, 1980; *Sempere et al.*, 1990]. These faults place Devonian on Cenozoic rocks, but their total displacement is uncertain.

[78] We tentatively favor the third model (Figure 14c), which is congruent with the structural and thermochronologic records. In considering these models, it is important to note that the proposed large-magnitude structures may link at depth with a deeper, NE directed décollement (Figure 14c), creating a crustal wedge geometry [e.g., *Roeder*, 1988; *Sempere et al.*, 1990; *McQuarrie and DeCelles*, 2001; *McQuarrie*, 2002; *McQuarrie et al.*, 2005a, 2005b].

### 8.4. Postshortening Exhumation

[79] On the basis of crosscutting relationships, most upper crustal shortening in the Cordillera Real (this study) and broader Eastern Cordillera of Bolivia [e.g., *Horton*, 2005] had ceased by $\sim 25$ Ma. It is difficult to reconcile this record with substantially increased cooling from late Miocene onward, raising the possibility that processes other than upper crustal shortening played a significant role in youthful exhumation of the central Andean plateau. Poten-

tial mechanisms include (1) lower crustal thickening by either thrust stacking [*Sheffels*, 1990; *McQuarrie and DeCelles*, 2001; *McQuarrie*, 2002], ductile deformation [*Isacks*, 1988], or underplating [*Baby et al.*, 1997] coeval with upper crustal shortening in the eastern foreland, (2) lithospheric delamination beneath the Altiplano–Eastern Cordillera boundary [*Lamb and Hoke*, 1997; *Beck and Zandt*, 2002; *Garzione et al.*, 2006], and (3) coupled erosional denudation and rock uplift along the eastern plateau margin [*Masek et al.*, 1994; *Horton*, 1999; *Montgomery et al.*, 2001].

[80] Although thermochronologic and structural results from this study are insufficient to distinguish between these models, regional considerations suggest important differences between the northern and southern parts of the central Andean plateau. Similar to our findings, AFT results across the Eastern Cordillera 600 km to the south at $\sim 21°$S indicate predominantly Eocene–Oligocene cooling related to crustal shortening [*Ege et al.*, 2003; *Ege*, 2004]. These data, however, lack signatures of the late Miocene and younger exhumation recorded in the Cordillera Real at $15.5-17.5°$S.

[81] Climate is similarly variable along strike, with markedly higher precipitation, erosional denudation, and topographic relief north of $\sim 17.5°$S contrasting with the arid, low-relief region to the south [e.g., *Masek et al.*, 1994; *Horton*, 1999; *Montgomery et al.*, 2001]. First-order controls on precipitation include zonal atmospheric circulation and orographic effects that focus precipitation along the eastern flank of the Andes north of $\sim 17.5°$S. This enhanced precipitation has promoted localized rock uplift, high relief, and headward retreat of the plateau margin [*Masek et al.*, 1994]. We propose that a pronounced north-south gradient in precipitation and erosion may explain rapid late Miocene and younger exhumation of the Cordillera Real in the absence of upper crustal shortening. The reason for a late Miocene inception of amplified exhumation is unknown, but may relate to climate change or deeper crustal/lithospheric tectonics.

## 9. Conclusions

[82] Integration of structure, geochronology, thermochronology, and sediment provenance demonstrates phases of rapid exhumation-induced cooling along the eastern margin of the central Andean plateau in Bolivia.

[83] 1. Mapping along three transects in the Cordillera Real reveals principally SW directed thrusts of the central Andean backthrust belt involving Paleozoic strata and Mesozoic-Cenozoic granites. Individual faults exhibit low magnitudes of displacement ($<2-5$ km). An estimated minimum cumulative slip of $\sim 20$ km, or $\sim 35\%$ NE-SW strain, is compatible with regional shortening estimates. Nevertheless, exposure of deep levels along the eastern flank of the central Andean plateau appears to require a deeper structure that may be linked to either SW or NE directed thrusts of the middle to lower crust.

[84] 2. Deformation timing is constrained by crosscutting relationships among granites, fold-thrust structures, and

basin fill. U-Pb analyses indicate Permo-Triassic and late Oligocene (~26 Ma) ages of granite crystallization. Permo-Triassic granites and lower Paleocene strata predate deformation, but the ~26 Ma Quimsa Cruz granite postdates most upper crustal shortening. Growth strata in the Luribay-Salla succession further indicate SW directed thrusting synchronous with pre-28 Ma sedimentation. Most fold-thrust deformation is therefore considered to be of Eocene-Oligocene age, in contrast to many previous studies suggesting strictly Neogene age deformation in the central Andes. The observed map relationships suggest no significant upper crustal deformation after ~25 Ma, but do not rule out the possibility of Neogene passive transport of upper crustal material above deeper structures.

[85] 3. As a measure of Cenozoic exhumation, the moderate-temperature (120–350°C) cooling history is determined by a combination of fission track, $^{40}Ar/^{39}Ar$, and MDD modeling results for 18 granite samples. The $^{40}Ar/^{39}Ar$ results for muscovite, biotite, and K-feldspar reveal a 45–40 Ma inception of rapid cooling, consistent with new and previous ZFT data [Benjamin et al., 1987]. Modeling of K-feldspar and AFT results indicate that rapid cooling continued throughout the late Eocene and Oligocene, with a reduction in cooling rates at ~26 Ma. These results agree with the structural record, in which most shortening preceded the Neogene. The erosional record of Eocene–Oligocene exhumation is preserved in the eastern Altiplano

basin, where 8 $^{40}Ar/^{39}Ar$ tuff ages and sediment provenance data reveal sedimentation between ~33 and 25 Ma.

[86] 4. AFT thermochronology and thermal modeling for 16 granite samples constrain the low-temperature (60–120°C) cooling history. Following an early to middle Miocene period of isothermal or slow cooling conditions, a phase of rapid cooling commenced at ~11 Ma. This young cooling episode postdated the dominantly pre-Neogene upper crustal shortening of the region, suggesting the potential role of exhumation mechanisms other than upper crustal deformation. Although there are several possibilities, the absence of rapid late Miocene cooling in the low-precipitation, low-erosion segment of the Eastern Cordillera in southern Bolivia at 21°S [Ege et al., 2003; Ege, 2004] suggests that the more erosive, high-precipitation climate north of 17.5°S may have driven youthful exhumation in the Cordillera Real.

## References

Allmendinger, R. W., T. E. Jordan, S. M. Kay, and B. L. Isacks (1997), The evolution of the Altiplano-Puna plateau of the central Andes, *Annu. Rev. Earth Planet. Sci.*, *25*, 139–174.

Anders, M. H., K. M. Gregory-Wodzicki, and M. Spiegelman (2002), A critical evaluation of late Tertiary accelerated uplift rates for the Eastern Cordillera, central Andes of Bolivia, *J. Geol.*, *110*, 89–100.

Arriagada, C., P. Roperch, P. R. Cobbold, and C. Mpodozis (2005), Numerical plan view restoration of the Bolivian orocline, paper presented at International Symposium on Andean Geodynamics, ORSTOM, Paris.

Baby, P., P. Rochat, G. Mascle, and G. Hérail (1997), Neogene shortening contribution to crustal thickening in the back arc of the central Andes, *Geology*, *25*, 883–886.

Baxter, E. F., D. J. DePaolo, and P. R. Renne (2002), Spatially correlated anomalous $^{40}Ar/^{39}Ar$ "age" variations in biotites about a lithologic contact near Simplon Pass, Switzerland: A mechanistic explanation for excess Ar, *Geochim. Cosmchim. Acta*, *66*, 1067–1083.

Beck, S. L., and G. Zandt (2002), The nature of orogenic crust in the central Andes, *J. Geophys. Res.*, *107*(B10), 2230, doi:10.1029/2000JB000124.

Benjamin, M. T. (1986), Fission-track ages on some Bolivian plutonic rocks: Implications for the Tertiary uplift and erosion history of the Altiplano-Cordillera Real, M.S. thesis, 58 pp., Dartmouth Coll., Hanover, N. H.

Benjamin, M. T., N. M. Johnson, and C. W. Naeser (1987), Recent rapid uplift in the Bolivian Andes: Evidence from fission-track dating, *Geology*, *15*, 680–683.

Carleson, W. D., R. A. Donelick, and R. A. Ketcham (1999), Variability of apatite fission-track annealing kinetics: I. Experimental results, *Am. Mineral.*, *84*, 1213–1223.

Carlier, G., G. Grandin, G. Laubacher, R. Marocco, and F. Megard (1982), Present knowledge of the magmatic evolution of the Eastern Cordillera, Peru, *Earth Sci. Rev.*, *18*, 253–283.

Crough, S. T. (1983), Apatite fission-track dating of erosion in the eastern Andes, Bolivia, *Earth Planet. Sci. Lett.*, *64*, 396–397.

Dallmeyer, R. D., and T. Rivers (1983), Recognition of extraneous argon components through incremental-release $^{40}Ar/^{39}Ar$ analysis of biotite and hornblende across the Grenvillian metamorphic gradient in southwestern Labrador, *Geochim. Cosmchim. Acta*, *47*, 413–428.

DeCelles, P. G., and B. K. Horton (2003), Early to middle Tertiary foreland basin development and the history of Andean crustal shortening in Bolivia, *Geol. Soc. Am. Bull.*, *115*, 58–77.

Donelick, R. A., R. A. Ketcham, and W. D. Carleson (1999), Variability of apatite fission-track annealing kinetics: II. Crystallographic orientation effects, *Am. Mineral.*, *84*, 1224–1234.

Dorbath, C., M. Granet, G. Poupinet, and C. Martinez (1993), A teleseismic study of the Altiplano and Eastern Cordillera in northern Bolivia: New constraints on a lithospheric model, *J. Geophys. Res.*, *98*, 9825–9844.

Ege, H. (2004), Exhumations- und Hebungsgeschichte der zentralen Anden in Südbolivien (21°S) durch Spaltspur-Thermochronologie en Apatit, Ph.D. thesis, 173 pp., Freie Univ., Berlin.

Ege, H., E. Sobel, V. Jacobshagen, E. Scheuber, and D. Mertmann (2003), Exhumation history of the central Andes of southern Bolivia by apatite fission track dating, *Rev. Tec. Yacimientos Petrol. Fis. Bolivianos*, *21*, 165–172.

Everndon, J. F., S. J. Kriz, and C. Cherroni (1977), Potassium-argon ages of some Bolivian rocks, *Econ. Geol.*, *72*, 1042–1061.

Farrar, E., A. H. Clark, D. J. Kontak, and D. A. Archibald (1988), Zongo–San Gabán zone: Eocene foreland

boundary of the central Andean orogen, northwest Bolivia and southeast Peru, *Geology*, *16*, 55–58.

Fitzgerald, P. G. (1994), Thermochronologic constraints on post-Paleozoic tectonic evolution of the central Transantarctic Mountains, Antarctica, *Tectonics*, *13*, 818–836.

Fitzgerald, P. G., and A. J. W. Gleadow (1988), Fission-track geochronology, tectonics and structure of the Transantarctic Mountains in northern Victoria Land, Antarctica, *Chem. Geol.*, *73*, 169–198.

Fitzgerald, P. G., R. B. Sorkhabi, T. F. Redfield, and E. Stump (1995), Uplift and denudation of the Alaska Range: A case study in the use of apatite fission track thermochronology to determine absolute uplift parameters, *J. Geophys. Res.*, *100*, 20,175–20,191.

Foster, D. A., T. M. Harrison, P. Copeland, and M. T. Heizler (1990), Effects of excess argon within large diffusion domains on K-feldspar age spectra, *Geochim. Cosmchim. Acta*, *54*, 1699–1708.

Garzione, C. N., P. Molnar, J. C. Libarkin, and B. J. MacFadden (2006), Rapid late Miocene rise of the Bolivian Altiplano: Evidence for removal of mantle lithosphere, *Earth Planet. Sci. Lett.*, *241*, 543–556, doi:10.1016/j.epsl.2005.11.026.

Gillis, R. J., B. K. Horton, and M. Grove (2004), Exhumation history and basin development along the eastern margin of the central Andean plateau, Bolivia, *Geol. Soc. Am. Abstr. Programs*, *36*, 433.

Gregory-Wodzicki, K. M. (2000), Uplift history of the central and northern andes: A review, *Geol. Soc. Am. Bull.*, *112*, 1091–1105.

Green, P. F. (1986), On the thermo-tectonic evolution of northern England: Evidence from fission track analysis, *Geol. Mag.*, *153*, 493–506.

Gubbels, T. L., B. L. Isacks, and E. Farrar (1993), High-level surfaces, plateau uplift, and foreland development, Bolivian central Andes, *Geology*, *21*, 695–698.

Harrison, T. M., M. T. Heitzler, O. M. Lovera, W. Chen, and M. Grove (1994), A chlorine disin-

fectant for excess argon released from K-feldspar during step heating, *Earth Planet. Sci. Lett.*, *123*, 95–104.

Heinrich, S. M. (1988), Geology and geochronology of the Zongo river valley, Cordillera Oriental, NW Bolivia, M.S. thesis, 185 pp., Queen's Univ., Kingston, Ont., Canada.

Henry, S. G., and H. N. Pollack (1988), Terrestrial heat flow above the Andean subduction zone in Bolivia and Peru, *J. Geophys. Res.*, *93*, 15,153–15,162.

Horton, B. K. (1999), Erosional control on the geometry and kinematics of thrust belt development in the central Andes, *Tectonics*, *18*, 1292–1304.

Horton, B. K. (2005), Revised deformation history of the central Andes: Inferences from Cenozoic foredeep and intermontane basins of the Eastern Cordillera, Bolivia, *Tectonics*, *24*, TC3011, doi:10.1029/2003TC001619.

Horton, B. K., B. A. Hampton, and G. L. Waanders (2001), Paleogene synorogenic sedimentation in the Altiplano plateau and implications for initial mountain building in the central Andes, *Geol. Soc. Am. Bull.*, *113*, 1387–1400.

Horton, B. K., B. A. Hampton, B. N. LaReau, and E. Baldellón (2002), Tertiary provenance history of the northern and central Altiplano (central Andes, Bolivia): A detrital record of plateau-margin tectonics, *J. Sediment. Res.*, *72*, 711–726.

Ingersoll, R. V., T. F. Bullard, R. L. Ford, J. P. Grimm, J. D. Pickle, and S. W. Sares (1984), The effect of grain size on detrital modes: A test of the Gazzi-Dickinson point-counting method, *J. Sediment. Petrol.*, *54*, 103–116.

Isacks, B. L. (1988), Uplift of the central Andean plateau and bending of the Bolivian orocline, *J. Geophys. Res.*, *93*, 3211–3231.

Kay, R. F., B. J. MacFadden, R. H. Madden, H. Sandeman, and F. Anaya (1998), Revised age of the Salla beds, Bolivia, and its bearing on the age of the Deseadan South American land mammal "age", *J. Vertebrate Paleontol.*, *18*, 189–199.

Kennan, L., S. Lamb, and C. Rundle (1995), K-Ar dates from the Altiplano and Cordillera Oriental of Bolivia: Implications for Cenozoic stratigraphy and tectonics, *J. S. Am. Earth Sci.*, *8*, 163–186.

Kennan, L., S. H. Lamb, and L. Hoke (1997), High-altitude palaeosurfaces in the Bolivian Andes: Evidence for late Cenozoic surface uplift, in *Palaeosurfaces: Recognition, Reconstruction and Palaeoenvironmental Interpretation*, edited by M. Widdowson, *Geol. Soc. Spec. Publ.*, *120*, 307–323.

Ketcham, R. A., R. A. Donelick, and W. D. Carleson (1999), Variability of apatite fission-track annealing kinetics: III. Extrapolation to geological time scales, *Am. Mineral.*, *84*, 1235–1255.

Ketcham, R. A., R. A. Donelick, and M. B. Donelick (2000), AFTSolve: A program for multi-kinetic modeling of apatite fission-track data, *Geol. Mater. Res.*, *2*, 1–32.

Kley, J., and C. R. Monaldi (1998), Tectonic shortening and crustal thickness in the central Andes: How good is the correlation?, *Geology*, *26*, 723–726.

Kontak, D. J., E. Farrar, A. H. Clark, and D. A. Arachibald (1990), Eocene tectono-thermal rejuvenation of an upper Paleozoic-lower Mesozoic terrane in the Cordillera de Carabaya, Puno, southeastern Peru, revealed by K-Ar and $^{40}$Ar/$^{39}$Ar dating, *J. S. Am. Earth Sci.*, *3*, 231–246.

Lamb, S., and L. Hoke (1997), Origin of the high plateau in the central Andes, Bolivia, South America, *Tectonics*, *16*, 623–649.

Lamb, S., L. Hoke, L. Kennan, and J. F. Dewey (1997), Cenozoic evolution of the Central Andes in Bolivia and northern Chile, in *Orogeny Through Time*, edited by J. P. Burg, and M. Ford, *Geol. Soc. Spec. Publ.*, *121*, 237–264.

Lancelot, J. R., G. Laubacher, R. Marocco, and U. Renaud (1978), U/Pb radiochronology of two granite plutons from the Eastern Cordillera (Peru): Extent of Permian magmatic activity and consequences, *Geol. Rundsch.*, *67*, 236–243.

Laslett, G. M., P. F. Green, I. R. Duddy, and A. J. W. Gleadow (1987), Thermal annealing of fission tracks in apatite 2. A quantitative analysis, *Chem. Geol.*, *65*, 1–13.

Lee, J. K. W. (1995), Multipath diffusion in geochronology, *Contrib. Mineral. Petrol.*, *120*, 60–82.

Lehmann, B. (1978), A Precambrian core sample from the Altiplano/Bolivia, *Geol. Rundsch.*, *67*, 270–278.

Lovera, O. M., F. M. Richter, and T. M. Harrison (1989), The $^{40}$Ar/$^{39}$Ar thermochronometry for slowly cooled samples having a distribution of diffusion domain sizes, *J. Geophys. Res.*, *94*, 17,917–17,935.

Lovera, O. M., M. Grove, T. M. Harrison, and K. I. Mahon (1997), Systematic analysis of K-feldspar $^{40}$Ar/$^{39}$Ar step heating results: I. Significance of activation energy determinations, *Geochim. Cosmchim. Acta*, *61*, 3171–3192.

Lovera, O. M., M. Grove, T. M. Harrison, and K. I. Mahon (2002), Systematic analysis of K-feldspar $^{40}$Ar/$^{39}$Ar step heating results: II. Relevance of laboratory argon diffusion properties to nature, *Geochim. Cosmchim. Acta*, *66*, 1237–1255.

Lutz, T. M., and G. Omar (1991), An inverse method of modeling thermal histories from apatite fission-track, *Earth Planet. Sci. Lett.*, *104*, 181–195.

MacFadden, B. J., K. E. Campbell, R. L. Cifelli, O. Siles, N. M. Johnson, C. W. Naeser, and P. K. Zeitler (1985), Magnetic polarity stratigraphy and mammalian fauna of the Deseadan (late Oligocene–early Miocene) Salla Beds of northern Bolivia, *J. Geol.*, *93*, 223–250.

Marsh, S. P., D. H. Richter, S. Ludington, E. Soria-Escalante, and A. Escobar-Diaz (1992), Geologic map of the Altiplano and Cordillera Occidental, Bolivia, in Geology and mineral resources of the Altiplano and Cordillera Occidental, Bolivia: U.S.G.S. and Servicio Geológico de Bolivia, *U.S. Geol. Surv. Bull.*, *1975*, plate 1.

Martinez, C. (1980), Structure et évolution de la chaîne hercynienne et da la chãcirc;ne andine dans le nord de la Cordillère des Andes de Bolivie, *Trav. Doc. ORSTOM*, *119*, 352 pp.

Masek, J. G., B. L. Isacks, T. L. Gubbels, and E. J. Fielding (1994), Erosion and tectonics at the margins of continental plateaus, *J. Geophys. Res.*, *99*, 13,941–13,956.

McBride, S. L., R. C. R. Robertson, A. H. Clark, and E. Farrar (1983), Magmatic and metallogenetic episodes in the northern tin belt, Cordillera Real, Bolivia, *Geol. Rundsch.*, *72*, 685–713.

McBride, S. L., A. H. Clark, E. Farrar, and D. A. Archibald (1987), Delimitation of a cryptic Eocene tectono-thermal domain in the Eastern Cordillera of the Bolivian Andes through K-Ar dating and $^{40}$Ar-$^{39}$Ar step-heating, *J. Geol. Soc. London*, *144*, 243–255.

McDougall, I., and T. M. Harrison (1999), *Geochronology and Thermochronology by the $^{40}$Ar/$^{39}$Ar Method*, 2nd ed., 269 pp., Oxford Univ. Press, New York.

McQuarrie, N. (2002), The kinematic history of the central Andean fold-thrust belt, Bolivia: Implications for building a high plateau, *Geol. Soc. Am. Bull.*, *114*, 950–963.

McQuarrie, N., and P. G. DeCelles (2001), Geometry and structural evolution of the central Andean backthrust belt, Bolivia, *Tectonics*, *20*, 669–692.

McQuarrie, N., B. K. Horton, G. Zandt, S. Beck, and P. G. DeCelles (2005a), Lithospheric evolution of the Andean fold-thrust belt, Bolivia, and the origin of the central Andean plateau, *Tectonophysics*, *399*, 15–37.

McQuarrie, N., J. B. Barnes, and T. A. Ehlers (2005b), The relationship between deformation and exhumation in the central Andean plateau, Bolivia, *Geol. Soc. Am. Abstr. Programs*, *37*, 271.

McRae, L. E. (1990), Paleomagnetic isochrons, unsteadiness, and uniformity of sedimentation in Miocene intermontane basin sediments at Salla, eastern Andean Cordillera, Bolivia, *J. Geol.*, *98*, 479–500.

Miller, J. F. (1988), Granite petrogenesis in the Cordillera Real, Bolivia and crustal evolution in the central Andes, Ph.D. thesis, 316 pp., Open Univ., London.

Miller, J. F., and N. J. Harris (1989), Evolution of continental crust in the central Andes: Constraints from Nd isotope systematics, *Geology*, *17*, 615–617.

Montgomery, D. R., G. Balco, and S. D. Willett (2001), Climate, tectonics, and the morphology of the Andes, *Geology*, *29*, 579–582.

Moore, M. A., and P. C. England (2001), On the inference of denudation rates from cooling ages of minerals, *Earth Planet. Sci. Lett.*, *185*, 265–284.

Newell, N. D. (1949), Geology of the Lake Titicaca region, Peru and Bolivia, *Mem. Geol. Soc. Am.*, *36*, 111 pp.

Pareja, J., C. Vargas, R. Suárez, R. Ballón, R. Carrasco, and C. Villaroel (1978), Mapa geológico de Bolivia y memoria explicative, scale 1:1,000,000, 27 pp., Yacimientos Petrol. Fis. Bolivianos and Serv. Geol. de Bolivia, La Paz.

Parsons, I., W. L. Brown, and J. V. Smith (1999), $^{40}$Ar/$^{39}$Ar thermochronology using alkali feldspars: Real thermal history or mathematical mirage of microtexture?, *Contrib. Mineral. Petrol.*, *136*, 92–110.

Roddick, J. C. (1978), The application of isochron diagrams in $^{40}$Ar-$^{39}$Ar dating: A discussion, *Earth Planet. Sci. Lett.*, *41*, 233–244.

Roddick, J. C., R. A. Cliff, and D. C. Rex (1980), The evolution of excess argon in Alpine biotites - An $^{40}$Ar-$^{39}$Ar analysis, *Earth Planet. Sci. Lett.*, *48*, 185–208.

Roeder, D. (1988), Andean-age structure of Eastern Cordillera (province of La Paz, Bolivia), *Tectonics*, *7*, 23–39.

Safran, E. B. (1998), Channel network incision and patterns of mountain geomorphology, Ph.D. thesis, 326 pp., Univ. of Calif., Santa Barbara.

Sandeman, H. A., A. H. Clark, and E. Farrar (1995), An integrated tectono-magmatic model for the evolution of the southern Peruvian Andes (13–20°S) since 55 Ma, *Int. Geol. Rev.*, *37*, 1039–1073.

Santos, J. O. S., L. A. Hartmann, H. E. Gaudette, D. I. Groves, N. J. Mcnaughton, and I. R. Fletcher (2000), A new understanding of the provinces of the Amazon craton based on integration of field mapping and U-Pb and Sm-Nd geochronology, *Gondwana Res.*, *3*, 453–488.

Sempere, T., G. Hérail, J. Oller, and M. G. Bonhomme (1990), Late Oligocene–early Miocene major tectonic crisis and related basins in Bolivia, *Geology*, *18*, 946–949.

Servicio Geológico de Bolivia (Geobol) (1993), Carta geologica de Bolivia, Ichoca (Hoja 6142), scale 1:100000, La Paz.

Servicio Geológico de Bolivia (Geobol) (1995), Carta geologica de Bolivia, Milluni (Hoja 5945), scale 1:100000, La Paz.

Servicio Geológico de Bolivia (Geobol) (1997), Carta geologica de Bolivia, Inquisivi (Hoja 6143), scale 1:100000, La Paz.

Servicio Nacional de Geología y Técnico de Minas and Yacimientos Petrolíferos Fiscales Bolivianos (2003), Mapa geologico de Bolivia, scale 1:100,000, La Paz.

Sheffels, B. M. (1990), Lower bound on the amount of crustal shortening in the central Bolivian Andes, *Geology*, *18*, 812–815.

Stüwe, K., L. White, and R. Brown (1994), The influence of eroding topography on steady state isotherms: Application to fission track analysis, *Earth Planet. Sci. Lett.*, *124*, 63–74.

Suárez, R., and E. Diaz (1996), Lexico estratigrafico de Bolivia, *Rev. Téc. Yacimientos Petrol. Fis. Bolivianos*, *17*(1–2), 7–227.

Willett, S. D. (1997), Inverse modeling of annealing of fission tracks in apatite. 1: A controlled random search method, *Am. J. Sci.*, *297*, 939–969.

Wörner, G., J. Lezaun, A. Beck, V. Heber, F. Lucassen, E. Zinngrebe, R. Rössling, and H. G. Wilke (2000), Precambrian and Early Paleozoic evolution of the Andean basement at Belen (northern Chile) and Cerro Uyarani (western Bolivia Altiplano), *J. S. Am. Earth Sci.*, *13*, 717–737.

Zeitler, P. K., and J. D. Fitz Gerald (1986), Saddle-shaped $^{40}$Ar/$^{39}$Ar spectra from young, microstruc-turally complex potassium feldspars, *Geochim. Cosmchim. Acta*, *50*, 1185–1199.

───────────

R. J. Gillis, Division of Geological and Geophysical Surveys, State of Alaska Department of Natural Resources, 3354 College Road, Fairbanks, AK 99709-3707, USA. (robert_gillis@dnr.state.ak.us)

M. Grove, Department of Earth and Space Sciences, University of California, 595 Charles Young Drive East, 3806 Geology Building, Los Angeles, CA 90095-1567, USA.

B. K. Horton, Department of Geological Sciences, Jackson School of Geosciences, University of Texas, 1 University Station C1100, Austin, TX 78712-0254, USA.